



Contents lists available at ScienceDirect

International Journal of Solids and Structures

journal homepage: www.elsevier.com/locate/ijsolstr

Analytical predictions, optimization, and design of a tensegrity-based artificial pectoral fin

K.W. Moored^a, T.H. Kemp^b, N.E. Houle^b, H. Bart-Smith^{b,*}

^a Department of Mechanical and Aerospace Engineering, Princeton University, Princeton, NJ 08544, USA

^b Department of Mechanical and Aerospace Engineering, University of Virginia, Charlottesville, VA 22904, USA

ARTICLE INFO

Article history:

Received 9 March 2011

Received in revised form 7 July 2011

Available online xxx

Keywords:

Tensegrity

Actuation

Morphing

Remote actuation

Active structure

ABSTRACT

For millions of years, aquatic species have utilized the principles of unsteady hydrodynamics to perform efficient, highly maneuverable and silent swimming motions. The manta ray, *Manta birostris*, has been identified as one such high performance species due to their ability to migrate long distances with low energy consumption, maneuver in spaces the size of their tip-to-tip wing span, produce enough thrust to leap out of the water and attain sustained swimming speeds of 2.8 m/s with low flapping frequencies. These characteristics make the manta ray an ideal candidate to emulate in the design of a bio-inspired autonomous underwater vehicle. The enlarged pectoral fins of the manta ray undergo complex motions that couple a curved spanwise deformation with a chordwise traveling wave to produce thrust and to maneuver. To produce an artificial pectoral fin that achieves this compound deformation while supporting large force generation, a tensegrity-based solution is developed. Various actuation strategies that are capable of matching these key kinematic features are explored and compared. Analytical solutions for active planar tensegrity beam structures are derived. These solutions allow for the direct calculation of optimal parameter values without the need to perform an exhaustive parametric study using a numerical solution. Moreover, the analytical solutions provide physical insight into the mechanics of tensegrity beams. Building on previous studies of active tensegrity structures, the loading response of different actuation strategies has been investigated analytically and is validated by a nonlinear numerical model and experiments. Optimal stiffness-to-mass and strength-to-mass strategies have been identified. Utilizing the analytical predictions for the optimal solution, an example design of a tensegrity-based artificial pectoral fin is shown. Structural performance metrics were calculated showing that the fin structure can closely match the kinematics of the manta ray, under external loading, using open-loop actuation of four actuators remotely located outside of the active structure. This approach costs minimal power consumption and shows the simple design of a high performance tensegrity-based artificial pectoral fin.

© 2011 Elsevier Ltd. All rights reserved.

1. Introduction and motivation

Active tensegrity structures are at the forefront of structural mechanics research. They have been utilized for active/deployable space structures (Furuya, 1992; Pinaud et al., 2003; Sultan and Skelton, 2003; Tibert, 2002; Tibert and Pellegrino, 2003) and adaptive architecture (Adam et al., 2007; Domer et al., 2005; Fest et al., 2003, 2004; Shea et al., 2002). Recent research has explored active tensegrity structures for the development of a morphing wing or pectoral fin that mimics the motions of the myliobatoid family, *Myliobatoidae*, which includes the manta ray, *Manta birostris*, and the cownose ray, *Rhinoptera bonasus* (Fig. 1) (Moored and Bart-Smith, 2007). Tensegrity structures offer high stiffness-to-mass and strength-to-mass ratios, large active deformations and low

energetic cost of actuation making them an ideal structural foundation for an artificial pectoral fin. This recent work has focused on embedded actuation (where the elements of the structure are directly replaced by actuators) but this approach requires many actuators for complex deformations, uses additional power to move the actuators themselves and imposes element size constraints on the structure. Alternatively, the actuators can be placed outside the structure and is referred to as *remote actuation*. This has only recently been modeled in tensegrity structures (Moored and Bart-Smith, 2009), to overcome the limitations of embedded actuation. However, deficiencies exist in understanding the loading response of this type of active structure, in defining optimal solutions for remote actuation, and in implementing these solutions in the design of an artificial pectoral fin. Thus this paper will address these deficiencies.

The first step in the development of a tensegrity-based artificial pectoral fin is to determine how static tensegrity structures trans-

* Corresponding author. Tel.: +1 4349240701.

E-mail address: hb8h@virginia.edu (H. Bart-Smith).

Nomenclature

α	prestress mode scaling	F_a	force on an actuating drum
ΔA	tensegrity cell vertical displacements	F_D	drag force
ΔT	change in tension	F_L	normal force
δ	horizontal nodal displacement	$F_{a,e}$	force on the actuator due to external loading
δ_a	actuator displacement	$F_{a,i}$	force on the actuator due to prestress reorientation
δ_a^*	additional actuator release	F_{fail}	breaking strength
δ_{tip}^{add}	additional tip displacement	h	Beam height
δ_{tip}^{std}	base displacement	k_r	relative stiffness
ϵ	strain	L	beam length
η_s	active structural efficiency	L/h	beam aspect ratio
λ_0	prestress	l_0	element length
λ_T	force density in a cable	M	applied bending moment
D	displacement calculation matrix	M_0	mass of a structure
N	elementary prestress modes	m	amplitude fitting parameter
S	clustering matrix	m_c	cable mass
\mathcal{K}_{bend}^1	bending stiffness of a single unit cell	m_s	strut mass
\mathcal{K}_{bend}	bending stiffness of a beam structure	MC	multiple cable-routed actuation
\mathcal{K}_{bend}/M	stiffness-to-mass ratio	N	number of unit cells
\mathcal{P}	power	P	vertical tip load
ρ	water density	P_{cr}	critical slackening load
ρ_c	cable density	P_{euler}	Euler buckling load
ρ_s	strut density	P_{fail}/M	strength-to-mass ratio
σ	stress	R	drum radius
σ_y	yield stress	r	drum radius at each cell attachment
τ_a	total actuator torque	r_c	cable radius
$\tau_{a,e}$	drum torque due to external loads	r_s	strut radius
$\tau_{a,i}$	drum torque due to pretension reorientation	S	platform area
θ	tensegrity cell rotation with respect to the horizontal	SC	single cable-routed actuation
θ_a	drum rotation angle	SR	strut-routed actuation
A	beam tip displacement	T_0	pretension
A/L	nondimensional tip amplitude	T_0^{opt}	optimal pretension scaling
A_c	area of the top and bottom cables	T_b	tension in the bottom cables
c	chord length	T_t	tension in the top cables
c_D	drag coefficient	U_f	velocity
D_c	cable diameter	W_e	work to move an loaded structure a distance A
E	modulus of elasticity for the cables	W_{struct}	work to move an unloaded structure a distance A
E_s	modulus of elasticity for the struts	x_f	flat coordinate positions
f	frequency		

late into active tensegrity structures. *Embedded actuation* was the first actuation strategy that facilitated this conversion by directly replacing individual elements with actuators (Djouadi et al., 1998), which can be applied to strut or cable elements. However, when active truss structures have cable elements (i.e. tensegrity structures) there are many more possibilities. As opposed to embedded actuation, *remote actuation* can be applied to tensegrity structures to migrate the actuators out of the structure relieving the limitations of embedded actuation.

To simplify the development of actuation concepts much of the discussion will be limited to two dimensional beam structures. However, the actuation strategies developed may be applied to three-dimensional structures as well. There are four possible actuation strategies that can be envisioned for a two-dimensional class 2 tensegrity beam structure¹ that produces an active bending mode (Fig. 2). Fig. 2a shows an example of embedded actuation applied to the optimal stiffness-to-mass planar tensegrity topology that uses three unit cells and aspect ratios (length-to-height of the structure) between three and nine (de Jager and Skelton, 2006). Fig. 2b–d shows three different remote actuation strategies. Strut-routed

(SR) actuation (Fig. 2b) utilizes a routed cable that runs along the struts of a tensegrity to reach an active element at a terminal location. Single cable-routed (SC) actuation (Fig. 2c) combines many active cable elements into a single cable that routes through the nodal points of the structure. Multiple cable-routed (MC) actuation utilizes multiple cables that overlap in some regions of the structure (Fig. 2d).

Embedded actuation has been considered by many researchers (Moored and Bart-Smith, 2007; Djouadi et al., 1998; Fest et al., 2004; Sultan et al., 2002; Masic and Skelton, 2005) and is modeled by the classic tensegrity equilibrium equations. It is the simplest solution to envision and can be applied to any type of tensegrity structure. However, embedded actuation uses many actuators for complex shape changes, adds mass to the moving structure (increasing the power consumption) and constrains the minimum element size to the size of an actuator.

Remote actuation has the advantage of migrating the actuators outside of the active structure to reverse the added mass and element size constraints due to embedded actuation. Also, it facilitates the connection of multiple active cable elements to a single actuator, thereby reducing the number of actuators necessary which reduces the cost of the system, the power consumption, the fabrication complexity and the controls complexity. Moreover,

¹ Class k structures have at most k struts attached to any node of the structure (Williamson et al., 2003).

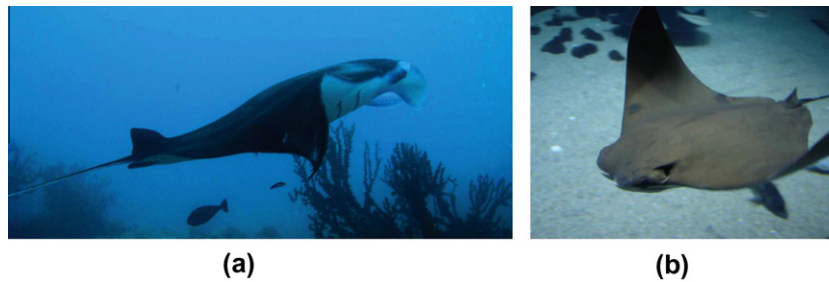


Fig. 1. Two species of the myliobatoid family: (a) *Manta birostris*, the manta ray and (b) *Rhinoptera bonasus*, the cownose ray.

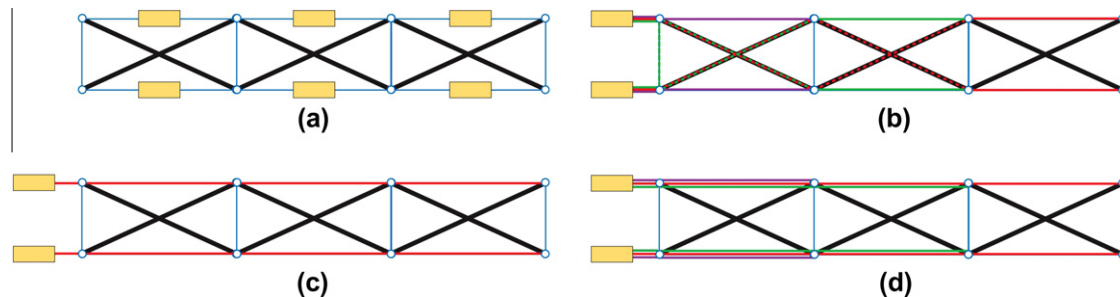


Fig. 2. The yellow boxes represent actuators: (a) an example of embedded actuation, (b) an example of strut-routed actuation, (c) an example of single cable-routed clustered actuation and (d) an example of multiple cable-routed clustered actuation. (For interpretation of the references to color in this figure legend, the reader is referred to the web version of this article.)

removing the actuators from the structure creates a more modular design for quicker, cheaper and simpler repairs. Lastly, in the case of an artificial pectoral fin, the actuators can be consolidated into a region where waterproofing can be more easily achieved.

The first remote actuation strategy, strut-routed (SR) actuation (Fig. 2b), has been applied as a fabrication method to achieve embedded actuation without embedding the actuators (Motro, 2003). In most cases, strut-routed actuation can be modeled using the classic equilibrium equations when the added length of cables is accounted for in the element stiffnesses. However, in mass optimal structures the classic equations will under predict the loads carried by the struts causing failure in a physical structure when it was not predicted. Consequently, a model to more accurately predict the mechanics of strut-routed actuation needs to be developed in order to accurately compare mass optimal structures. Also, strut-routed actuation has many limitations. It requires a path of connecting struts from the actuator to the active element location, which restricts this solution to class 2+ structures. Furthermore, there is typically a drop-off in the bending stiffness as the number of elements increases due to the increasing active cable length and thus the increasing compliance of those elements drops the bending stiffness. Moreover, when the cables are redirected at the connection of two struts, static friction can be high due to the pretension in the cables when the redirection mechanism is not near frictionless. Lastly, structures with strut-routed actuation tend to have many prestress states and thus require many pretension mechanisms making the structure difficult to fabricate as the number of elements increases.

The second remote actuation strategy, single cable-routed (SC) actuation (Fig. 2c), has been investigated in the context of deployable pantographic structures (Kwan et al., 1993; Kwan and Pellegrino, 1994; You and Pellegrino, 1996; You and Pellegrino, 1997) and in some deployable tensegrity structures (Smaili and Motro, 2005) as a method for the application and removal of self-stress to deploy and collapse a structure. It has only recently been applied as a strategy to actively deform a tensegrity structure (Moored and Bart-Smith, 2009). At first glance, the SC solution is the ideal choice for an actu-

ation strategy. It offers all of the advantages of a remote actuation strategy while being able to be applied to any class of tensegrity structure (no strut-to-strut path required), reduce the number of prestress states to a single global state greatly simplifying the fabrication process and theoretically has zero static friction for actuation, due to a straight cable routing path along the exterior of a beam structure.

The third remote actuation strategy, multiple cable-routed (MC) actuation (Fig. 2d), is a novel concept and is absent from the literature. The generalized tensegrity equilibrium equations (Moored and Bart-Smith, 2009) can be used to accurately model this actuation strategy. At first glance, this strategy would be the second best choice as an actuation strategy. It offers the remote actuation advantages, has the potential to be applied to any class of tensegrity structure, and theoretically has zero static friction for actuation. However, since there are multiple cables, each cable would need to be pretensioned which does not allow for a reduction of the number of prestress states as in the SC solution.

Naturally many question arise. How is the actuation and loading response of the structures affected by the application of a remote actuation strategy? Do all of the strategies admit feasible prestress states? Do they all create stable structures? Which of the four possible actuation strategies is the optimal solution for an artificial pectoral fin?

To answer these questions, the paper is organized in the following manner. Section 2 derives analytical predictions for a tensegrity beam utilizing embedded actuation and then expanded to the MC and SR solutions. The analytical solutions can act as simple design equations and provide physical insight into how the structural response is dependent on the parameters, which is useful for developing intuition. Section 3 validates the analytical and numerical solutions through a comparison with experimental results. Section 4 explores the different routing solutions (Fig. 2b–d) and compares the loading response of optimal beam structures utilizing the analytics and the numerical model developed in Moored and Bart-Smith (2009). Section 5 presents an example design of a tensegrity-based artificial pectoral fin with the optimal remote actuation

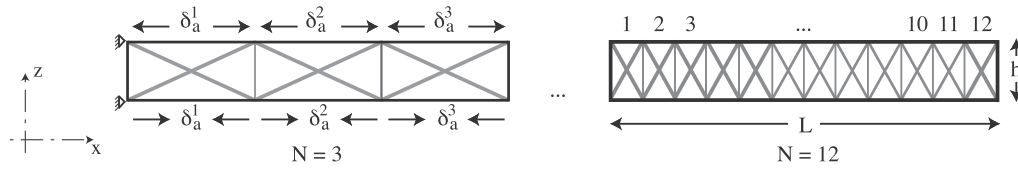


Fig. 3. A tensegrity beam structure with embedded actuation has an aspect ratio, L/h , and is composed of a number of cells, N . The actuation displacements, δ_a^i , are applied to individual elements on the top and bottom of the structure to enable the beam with an active bending deformation.

strategy employed (MC) by utilizing the analytical solutions. Lastly, Section 6 summarizes the conclusions drawn from this study.

2. Analytical mechanics

In this section analytical solutions are derived from first principles for the actuation and loading response of an active class 2 planar tensegrity beam. These solutions allow for the direct calculation of parameters to achieve a given structural performance, elucidate optimal pretensioning and provide insight into the mechanics of active tensegrity beam structures. Furthermore, the predictions quantify how the structural performance of these beams varies due to scalings in the design parameters (i.e. number of cells, aspect ratio, pretension, and material properties). These analytical solutions are used in the design of active tensegrity beams, which act as the structural foundation for an artificial pectoral fin.

To develop an analytical approach, consider a class 2 tensegrity beam with embedded actuation (Fig. 3). This beam has an aspect ratio, L/h , and can be composed of any number of cells, N , from 1 to ∞ within the space defined. For a planar beam to be actively deformed in bending the top and bottom elements of the structure are defined as the active elements. Furthermore, it is assumed that there is a one-to-one antagonistic relationship between the top and bottom cables allowing for an active bending mode without strain energy being induced into the structure (first-order approximation). The cells of the structure are numbered from root to tip ($1 \rightarrow N$) and are denoted by superscripts on the variables.

2.1. Actuation response

First, the actuation response of the structure to an actuator displacement of the active cables is considered. The actuation response is the deformation field of the structure under the actuation of the cable elements, δ_a^j . Fig. 4 shows how a single tensegrity cross structure deforms from a defined actuator displacement.

When a second cell is attached onto the first cell its neutral axis would immediately have an angle relative to the horizontal equal to 2θ . This comes from the addition of the previous cell's neutral axis angle and the angle of the interface between the two cells. Moreover, the second cell is assumed to also be actuated by δ_a creating an angle 3θ with the horizontal. Continuing on with the addition of a third cell, an angle of 5θ between the neutral axis of that cell and the horizontal is created. As N increases the N th cell attains an angle of $(2N - 1)\theta$ with the horizontal. Furthermore, as the number of cells increases the length of an individual cell decreases and is L/N . This leads to an overall amplitude of deflection of the beam structure to be the following:

$$A = \frac{L}{N} \sin(\delta_a^1/h) + \frac{L}{N} \sin(2\delta_a^1/h + \delta_a^2/h) + \frac{L}{N} \sin(2\delta_a^1/h + 2\delta_a^2/h + \delta_a^3/h) + \dots$$

$$A = \frac{L}{N} \sum_{j=1}^N \sin \left[\sum_{i=1}^{j-1} (2\delta_a^i/h + \delta_a^j/h) \right] \quad (1)$$

In general, the actuator displacements, δ_a^j , can be calculated for any set of cell displacements, ΔA^j

$$\delta_a = h \mathbf{D}^{-1} \sin^{-1} \left(\frac{\Delta \mathbf{A} \mathbf{N}}{L} \right), \quad \text{where } A = \sum_{j=1}^N \Delta A^j \text{ and } D_{ij} = \begin{cases} 0, & i < j \\ 1, & i = j \\ 2, & i > j \end{cases} \quad (2)$$

When all of the actuator displacements are equivalent ($\delta_a^j = \delta_a$) then, the terms of the series (Eq. (1)) become $\sin(\theta)$, $\sin(3\theta)$, $\sin(5\theta)$, etc. This series converges to the following nonlinear equation in δ_a .

$$A = \frac{L}{N} \csc \left(\frac{\delta_a}{h} \right) \sin^2 \left(\frac{N\delta_a}{h} \right) \quad (3)$$

When $\delta_a^j = \delta_a$, the terms in Eq. (1) can be simplified using some trigonometric identities and the small angle assumption to give $\sin(\delta_a/h) \approx \delta_a/h$, $\sin(3\delta_a/h) \approx 3\delta_a/h$ and $\sin(5\delta_a/h) \approx 5\delta_a/h$. This produces the series $\sum_{j=1}^N (2j - 1)/N$ that can be shown to be equal to N , giving the approximate relationship between an actuator displacement and the tip displacement of the beam structure

$$\delta_a \approx \frac{A}{N} \left(\frac{h}{L} \right) \quad (4)$$

The exact solutions (Eqs. (2) and (3)) allow for direct calculation of the necessary actuator strokes required to match the deformed structure to a biological displacement field. Eq. (4) acts as an estimation for the actuator strokes necessary, but more importantly shows a clear and concise relationship among the parameters A , N , and L/h .

The small angle approximation used in Eq. (4) begins to break down as the non-dimensional tip amplitude, A/L , gets too large ($A/L \approx 1/2$). As can be seen in Fig. 5a, the estimation (solid line) approaches 10% error for a tip amplitude that is half of the span length when compared to the numerical model presented by Moored and Bart-Smith (2009). Of course, the nonlinear equation (Eq. (3)) can be solved to predict higher amplitude motion (Fig. 5b) which can be seen to match well with the numerical model. The nonlinear analytical prediction assumes that there is no strain in the structure during actuation while the numerical model does not make this assumption, leading to some discrepancy between the analytical prediction and the numerical solution, especially at low values of N . For instance, at the worst case calculated ($N = 1$, $L/h = 6$ and $A/L = 2/3$), the analytical prediction has an error of 7.4%.

2.2. Element force response

Next, consider a cantilever tensegrity beam with a vertical tip load, P , acting on it (Fig. 6a). The beam can be broken into its individual cells and the change in tension in the top and bottom cables can be calculated for each section. It is assumed that due to a point load at the tip of the beam, the tension will increase in the top cables and have an equal but opposite change in the bottom cables (Fig. 6c).

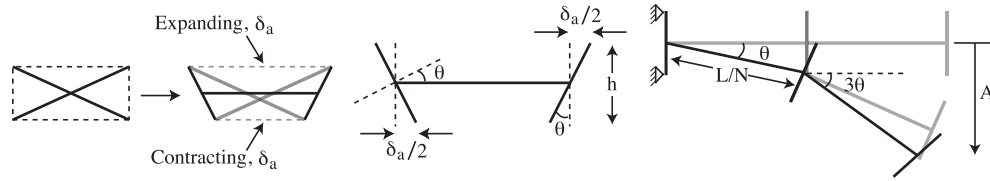


Fig. 4. The actuator displacement, δ_a , causes the vertical elements of a single tensegrity cell to rotate θ . When multiple cells are attached together and actuated there is a progression of the angle of a cell with the horizontal.

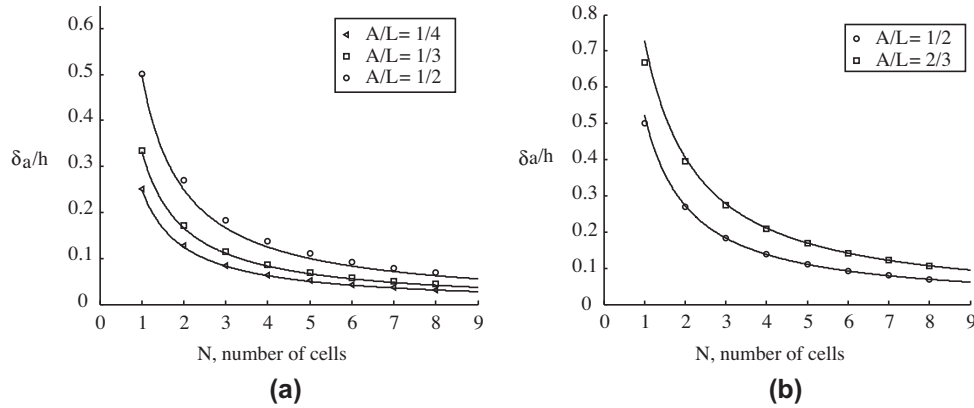


Fig. 5. Normalized actuator stroke as a function of N for varying values of A/L when $\delta_a^i = \delta_a$. The solid lines are the analytical predictions while the points are the numerical simulations. The aspect ratio is $L/h = 6$. (a) Shows the approximation (Eq. (4)) and (b) shows high amplitude motion (Eq. (3)).

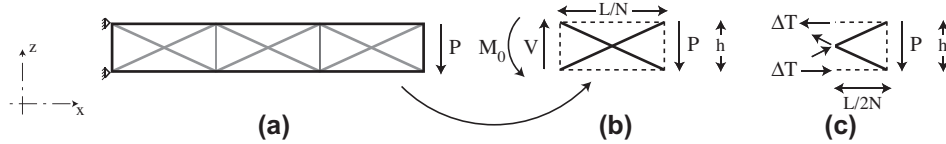


Fig. 6. Diagram of (a) a cantilever tensegrity beam under a point load at the tip, (b) forces and moments acting on the tip cell and (c) a section cut through the center of the cell showing the change in forces.

By progressively evaluating each cell from tip to root it is found that the moment at the interface of two cells (which is applied as a force couple at the nodes) increases linearly from tip to root as would be expected from beam theory. Then the method of sections can be applied to an individual cell by making a cut through the center of the cell (Fig. 6c). Summing moments about the center allows for a solution to the change in tension due to a tip load in a given cell. It is found that the j th cell will have the following change in tension

$$\Delta T_j = \left(\frac{2N - 2j + 1}{2N} \right) \frac{PL}{h} \quad (5)$$

By incorporating the pretension in the cables, the force on an actuator due to external loading at the tip is determined by

$$F_{a,e}^j = T_0^j \pm \left(\frac{2N - 2j + 1}{2N} \right) \frac{PL}{h} \quad (6)$$

The tension increases (+) for the top cables and decreases (–) for the bottom cables when the tip load is applied in the $-z$ direction. By using the principle of superposition this solution can be expanded to estimate the force on the actuator due to a distributed load

$$F_{a,e}^j = T_0^j \pm \sum_{i=j}^N \left(\frac{2N - 2j + 1}{N} \right) \frac{P_i L}{h} \quad (7)$$

The load P_i acts in the $-z$ direction on the right side of the i th cell. Numerically this load is decomposed from P_i into $P_i/2$ and applied to the top and bottom nodes of the right side of a cell.

2.3. Critical slackening load

The change in tension in the top and bottom cables due to an applied loading (Eq. (5)) directly leads to a critical load at which a cable goes slack. Under a tip load, P , in the $-z$ direction there is a reduction in tension in the bottom cable of the j th cell as stated in Eq. (5). When the reduction in tension is equal to the pretension then the cable has reached its critical slackening load.

$$P_{cr}^j = \left(\frac{2N}{2N - 2j + 1} \right) T_0^j \frac{h}{L} \quad (8)$$

For equal pretension in all of the bottom and top cables, the root cell will reach the critical slackening load before any other cell under the described applied tip load. When this cable goes slack, the bending stiffness has a discontinuity and approximately drops in half. Once the first cable goes slack the forces in the tensegrity are redistributed such that the critical slackening load prediction (Eq. (8)) is no longer valid. In order for all the cables to go slack simultaneously under a prescribed tip load a non-uniform distribution of pretension is applied. This distribution of optimal pretension can be directly calculated from Eq. (8) based on an applied tip load.

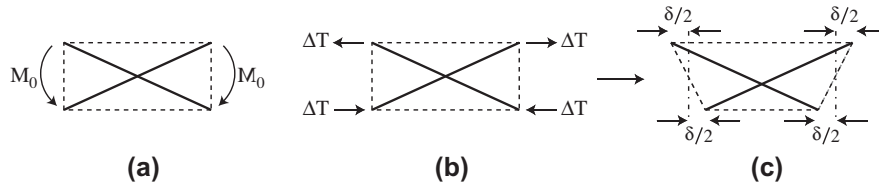


Fig. 7. (a) Moments on a single tensegrity cell can be applied as (b) a force couple. This loading scenario causes (c) displacements of the nodes.

2.4. Optimal pretensioning

The optimal amount of pretension in the top and bottom cables of a cell decreases from root to tip. The optimal pretension for each cell of a three-cell beam are 5, 3 and 1 times the pretension in the tip section and for a four-cell beam they are 7, 5, 3 and 1 times the pretension in the tip cell. This pattern continues as $2N - 2j + 1$ from root to tip as j goes from $1 \rightarrow N$. Assuming that the relative values of pretension are set in this pattern, the optimum scaling of the pretension for the tip cell can be found such that all of the bottom cables are on the cusp of going slack under a tip load, P , to minimize the amount of pretension in the structure

$$T_0^{opt} = \frac{PL}{2Nh} \quad (9)$$

Thus the optimal pretensioning, for an embedded actuation tensegrity beam, in each cell from root to tip set at $[(2N - 1), \dots, (2N - 2j + 1), \dots, 3, 1]T_0^{opt}$.

2.5. Deformation response

To determine the bending stiffness of a single tensegrity structure, consider the response of the structure due to applied bending moments, M_0 (Fig. 7). These bending moments are applied to a tensegrity structure as a force couple as seen in Fig. 7b. By applying this loading scenario to the stiffness matrix (evaluated symbolically) defined in Moored and Bart-Smith (2009) and Masic et al. (2005) of a single tensegrity cell, the resistive change in tension in the top and bottom cables is the following:

$$\Delta T = \frac{EA_c}{L} \delta + \frac{2T_0}{L} \delta \quad (10)$$

The modulus of elasticity of the cables is E while the area of the top and bottom cables is A_c . As stated before, a change in tension in the top and bottom cables can be related to an applied tip load (Eq. (5)). Thus, the change in tension due to the bending moments can be related to a tip load

$$\frac{PL}{2h} = \frac{EA_c}{L} \delta + \frac{2T_0}{L} \delta \quad (11)$$

Furthermore, the horizontal nodal displacements, δ , due to the bending moments can be related to a vertical tip displacement through Eq. (4) ($\delta = Ah/L$). By combining Eqs. (4) and (11), the bending stiffness of a single cell, \mathcal{K}_{bend}^1 , can be determined by solving for P/A

$$\mathcal{K}_{bend}^1 = 2 \left(\frac{EA_c}{L} + \frac{2T_0}{L} \right) \left(\frac{h}{L} \right)^2 \quad (12)$$

If all cells have equal length, then the length of one cell is L/N . This correction alters the relationship of the change in tension due to a bending moment ($\Delta T = [NEA_c/L + 2NT_0/L]\delta$). The change in tension of each cell progressively increases from tip to root as described earlier. The change in tension relation (Eq. (5)) can be used for each successive cell to calculate the vertical displacement of that cell. Furthermore, as shown in Eq. (1) the root cell has a greater influence on the bending deflection than the cells towards the tip. By including this, it can be shown that the first-order bending stiffness of a tensegrity beam with any number of cells is the following:

$$\mathcal{K}_{bend} = \frac{N^3 \mathcal{K}_{bend}^1}{\sum_{j=1}^N (2N - 2j + 1)^2} = \frac{6N^2}{4N^2 - 1} \left(\frac{EA_c}{L} + \frac{2T_0}{L} \right) \left(\frac{h}{L} \right)^2 \quad (13)$$

This first-order bending stiffness prediction is in excellent agreement with the numerical model (Fig. 8) over four orders of magnitude in relative stiffness,

$$k_r = EA_c/2T_0 \quad (14)$$

which is the ratio of the bending stiffness due to the material properties compared to the pretensional stiffness. This parameter is similar to the yield strain criteria used in Masic et al. (2006) to find that high yield strain materials can have a greater pretensional contribution to the bending stiffness. Low values of relative stiffness means that the pretension dominates the bending stiffness (Eq. (14)) while high values means that the material properties dominate the response. Moreover, since T_0/A_c is the stress in a cable, σ , and $\sigma/E = \epsilon$, the relative stiffness parameter can be rearranged to reflect the amount of strain in the cables due to pretension, $k_r = 1/2\epsilon$. Thus at the lowest relative stiffness investigated ($k_r = 1/10$) the cables must be strained to 500%, well beyond the point where linearity

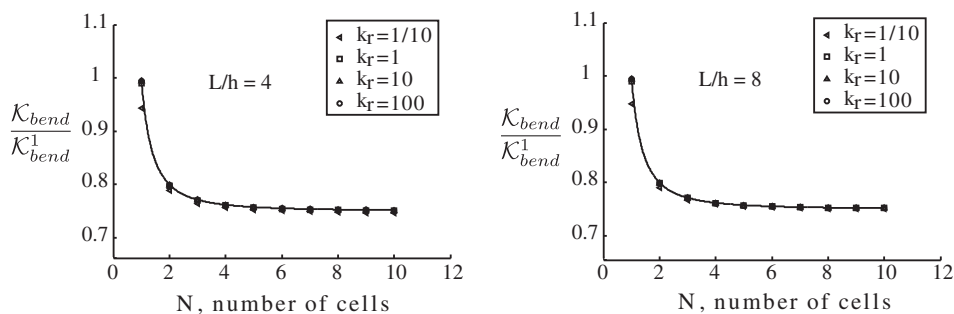


Fig. 8. The analytical prediction for the bending stiffness (solid line) has excellent agreement with the numerical model (points) over four orders of magnitude of relative stiffness, k_r . The left graph has an aspect ratio of $L/h = 4$ while the right graph has an aspect ratio of $L/h = 8$.

holds for all known materials. To fabricate a structure in this range, highly elastic materials or highly compliant springs would be necessary. Yet even at this limit the bending stiffness prediction is in excellent agreement with the numerical model. There is also excellent agreement for any number of cells and over a range of aspect ratios. However, the first-order bending stiffness prediction begins to break down for beams with low aspect ratios ($L/h < 2$).

Murakami (2001) shows that the natural frequencies of eigenmodes that cause first-order extension of the elements are not significantly affected by changes in pretension. However, this is only true for high values of relative stiffness. For low values of relative stiffness, the stiffness and thus the natural frequency of deformation modes that cause extension can be significantly affected by changes in pretension. A structure with a relative stiffness between 1 and 1/10 would be able to actively vary its bending stiffness by varying the amount of pretension in the structure without changing the geometry. This property is unique to prestressed structures and may be utilized to actively vary the natural frequency of the structure (Murakami, 2001). Furthermore, the bending stiffness formula (Eq. (13)) also shows that the number of cells does not have a significant effect on the bending stiffness (i.e. the aspect ratio of an individual cell does not matter) and the greatest way to vary the bending stiffness is to vary the aspect ratio of the entire beam. The stiffness formula relates the parameters N , E , A_c , T_0 , L , and L/h , so that if five of these parameters are known and there is a target bending stiffness, the sixth parameter may be directly calculated instead of using an iterative optimization of the numerical model.

2.6. Pretensional actuation resistance

Lastly, the amount of force that is necessary to actuate the structure under no external load is examined. There are two contributions to resist actuation in a one-to-one antagonistic actuation scenario. The first-order contribution comes from the reorientation of pretension vectors (Fig. 9), while a higher order contribution comes from strain induced in the structure during actuation. It can be seen in Fig. 9 that when an actuator displacement, δ_a , is applied to a single tensegrity cell all of the elements of the structure preserve their initial orientations except the vertical cables and to first-order none of the elements are strained. Since there is pretension in the vertical cables, the reorientation of those force vectors causes a component of the vector to resist the displacement of the top cable and the bottom cable. The combination of these internal forces leads to a first-order resistance to actuation of

$$\Delta F_{a,i} = T_0 \frac{h}{L} \left(\frac{\delta_a}{h} \right) \quad (15)$$

This resistive force can easily be expanded to a tensegrity beam of any number of cells. The length of a cell goes to L/N and the first-order force on the j th actuator is the following:

$$F_{a,i}^j = NT_0^j \frac{h}{L} \left(\frac{\delta_a^j}{h} \right) \quad (16)$$

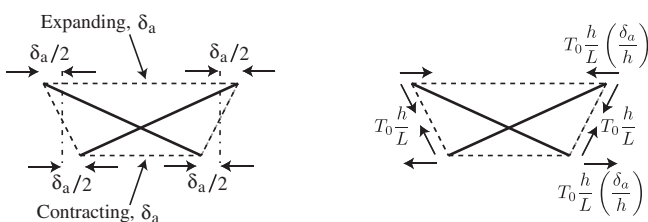


Fig. 9. When a tensegrity cell is actuated the first-order effect is the reorientation of the pretension vectors to resist the actuation.

In this equation it is assumed that the pretension in each cell is the same. The last contribution to the actuator force for an unloaded tensegrity beam is the strain induced in the structure while antagonistically actuating the structure. This contribution is difficult to estimate as it is a higher-order contribution. Instead the nonlinear numerical model can be employed to measure the amount of force on the actuator. Knowing the amount of force acting on the actuator from both the first-order contribution and the higher-order contribution helps determine the actuator requirements necessary to carry that load. Also, with the first-order contribution known, the one-to-one antagonistic strategy can be modified so that more cable is released than pulled in. The additional release necessary, δ_a^* to eliminate the resistive force due to pretension reorientation is the following:

$$\delta_a^* = \frac{2T_0^j h}{EA_c} \left(\frac{\delta_a^j}{h} \right) \quad (17)$$

This displacement must be applied for each cell to incur a zero first-order contribution to the energy of actuation. If there are different levels of pretension in each cell then the additional release displacements will vary from cell to cell.

2.7. Mechanics of remote actuation strategies

The analytical solutions derived in this section were for a structure utilizing an embedded actuation strategy. It will be shown in Section 4, that the choice of routing strategy does change the mechanics formulation. Equally, the analytical solutions for the MC and SR strategies are different than the embedded actuation case. Table 1 is a compilation of the analytical solutions based on the remote routing strategy employed. The SC solution is not shown as it is not recommended in load-bearing applications (Section 4). All of the design equations were derived using similar methodologies to the embedded actuation case, however all of the active cable elements are assumed to be attached to an actuating drum (Fig. 10). If a pull-release ratio other than one-to-one were desired, then the round drum could be replaced with an elliptical cam device.

An actuator is attached to a drum where all of the top elements are connected to the top side of the drum, while the bottom elements are connected to the bottom side of the drum (Fig. 10b). The force on the actuating drum, F_a , at a given radius, is the difference in tension between the top and bottom cables of a cell ($F_a = T_t - T_b$). The balancing of the forces in the top cables with the forces in the bottom cables eliminates the pretension force on the actuator.

The actuation response of the two remote actuation strategies differs. If each cell of a beam structure is actuated some amount (δ_a), utilizing the MC solution, then only the root cell will bend while the other cells will hold their static neutral positions (Fig. 11a). For a three cell beam using the MC solution, the cell actuator displacements must be $[\delta_a, 2\delta_a, 3\delta_a]$ from root cell to tip cell to match the structural displacement field of the SR solution when cell actuator displacements of $[\delta_a, \delta_a, \delta_a]$ are applied (Fig. 11c).

Even though the actuator strokes are higher for the MC solution, the forces in the cables due to external loading drop in the same ratios, exhibiting a typical mechanical advantage tradeoff. Furthermore, since the active cable elements are attached to a drum that is actuated by one actuator, the differences in stroke for the MC solution can be achieved by having a drum with different radii for each cell. For a three cell beam, the radii would be $[R, 2R, 3R]$ to have the MC displacement field match the SR displacement field with a constant radius drum (Fig. 11). Since the radius of the drum increases for each active cell in the MC solution there is a larger moment on the actuating drum from each cell. The reduction in the forces in

Table 1

[Summary of design equations] Design equations for both actuation strategies: multiple cable-routing (MC) and strut-routing (SR).

MC (drum)	SR (drum)
$P_{cr}^j = \begin{cases} NT_0^j \frac{h}{L} & \text{if } j \neq N \\ 2NT_0^j \frac{h}{L} & \text{if } j = N \end{cases}$	$P_{cr}^j = \frac{2N}{2N-2j+1} T_0^j \frac{h}{L}$
Optimal pretension	Optimal pretension
$T_0 = [2, 2, 2, \dots, 1] T_0^{opt}$ $T_0^{opt} = \frac{PL}{2Nh}$	$T_0 = [2N-1, \dots, (2N-2j+1), \dots, 3, 1] T_0^{opt}$ $T_0^{opt} = \frac{PL}{2Nh}$
$\mathcal{K}_{bend} = \frac{2N^2}{2N-1} \left(\frac{EA_c}{L} + \frac{2T_0}{L} \right) \left(\frac{h}{L} \right)^2$	$\mathcal{K}_{bend} = \frac{12N^2}{\alpha(N)+8N^2-2} \left(\frac{EA_c}{L} + \frac{2T_0}{L} \right) \left(\frac{h}{L} \right)^2$ $\alpha(N) = \sqrt{(Nh/L)^2 + 1} (2N^3 - 4N^2 + N + 1)$
Exact curvature case	Exact curvature case
$\delta_a = \mathbf{D}^{-1} h \sin^{-1} \left(\frac{\Delta AN}{L} \right)$	$\delta_a = \mathbf{D}^{-1} h \sin^{-1} \left(\frac{\Delta AN}{L} \right)$
$D_{ij} = \begin{cases} 1 & i=j \text{ or } i-1=j \\ 0 & \text{otherwise} \end{cases}$	$D_{ij} = \begin{cases} 0 & i < j \\ 1 & i = j \\ 2 & i > j \end{cases}$
$\theta_a = \delta_a^j / r^j, \quad r^j = \delta_a^j / \delta_a^1$	$\theta_a = \delta_a^j / r^j, \quad r^j = \delta_a^j / \delta_a^1$
Approximate curvature case	Approximate curvature case
$\frac{\delta_a^j}{h} \approx \frac{j}{N} \frac{A}{L}, \quad r^j = jR$ $\theta_a \approx \frac{h}{NR} \frac{A}{L}$	$\frac{\delta_a^j}{h} \approx \frac{A}{NL}, \quad r^j = R$ $\theta_a \approx \frac{h}{NR} \frac{A}{L}$
$F_{a,e}^j = \begin{cases} T_0^j \pm \frac{PL}{Nh} & \text{if } j \neq N \quad (\text{Top cables } (+)) \\ T_0^j \pm \frac{PL}{2Nh} & \text{if } j = N \quad (\text{Bottom cables } (-)) \end{cases}$	$F_{a,e}^j = T_0^j \pm \frac{2N-2j+1}{2N} \frac{PL}{h}$ (Top cables +, bottom cables -)
when, $r^j \approx jR$	when, $r^j \approx R$
$\tau_{a,i} = 2N^3 T_0^{opt} \frac{R^2}{L} \theta_a \quad (\text{optimal pretension})$ $\tau_{a,e} = (F_{a,top}^j - F_{a,bot}^j) r^j, \quad \tau_{a,e} = NPR \frac{L}{h}$	$\tau_{a,i} = 2N^3 T_0^{opt} \frac{R^2}{L} \theta_a \quad (\text{optimal pretension})$ $\tau_{a,e} = (F_{a,top}^j - F_{a,bot}^j) R, \quad \tau_{a,e} = NPR \frac{L}{h}$

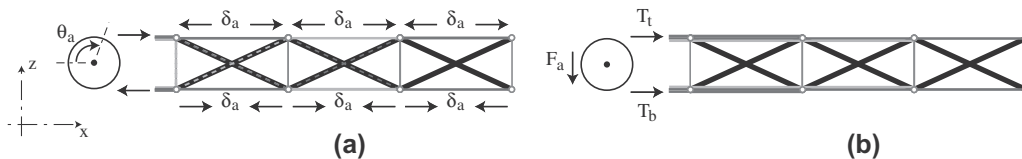


Fig. 10. (a) Shows the drum rotating an angle θ_a which causes an expansion of δ_a in the top cables and a contraction of δ_a in the bottom cable of a SR beam. (b) A MC beam has the top cable elements attached to the top side of the drum while the bottom cables are attached to the bottom side of the drum. The net force F_a is the difference between the tension in the top cables, T_t , and the bottom cables, T_b .

the elements due to a tip load perfectly offsets the increase in stroke necessary, such that both the MC and SR solution take the same amount of work done by the actuator to move a tip load, P , a given distance, A .

Note that determining the optimal pretension for the SR solution is a straightforward analogy to the embedded actuation case, but for the MC solution it is a little more tricky. With the MC solution there are multiple cables running over the top and bottom of

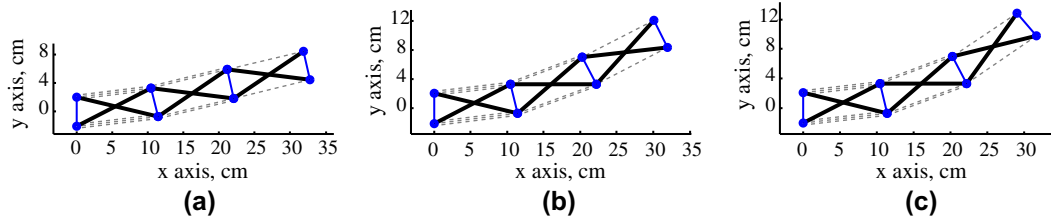


Fig. 11. Structural displacement field, using MC strategy, due to an actuator displacement (a) of $[\delta_a, \delta_a, \delta_a]$, (b) of $[\delta_a, 2\delta_a, 2\delta_a]$ and (c) of $[\delta_a, 2\delta_a, 3\delta_a]$.

each cell except the tip cell. Thus, the sum of the pretensions in all of the cables running over a cell must add to the ratios defined above. This means that the cable that runs to the tip cell must have a pretension of T_0^{opt} found from Eq. (9). The next cell over from the tip already has a pretension of T_0^{opt} from the cable running to the tip so the other cable terminating at the end of the second cell must have a pretension of $2T_0^{opt}$ for the second cell to have a total pretension of $3T_0^{opt}$. Furthermore, the first cell already has a pretension of $3T_0^{opt}$ from the two cables running to the second and third cells, so the cable terminating at the end of the first cell must also have a pretension of $2T_0^{opt}$ to sum to a total of $5T_0^{opt}$ for the first cell. This pattern continues for any number of cells such that each cable should have a pretension of $2T_0^{opt}$ except for the cable that routes all the way to the last cell at the tip which should have a pretension of T_0^{opt} . This is beneficial since the cable diameters do not need to increase towards the root of the structure in order to carry the higher pretension loads without yielding.

The analytical solutions (Table 1) provide insight into the mechanics of the remote actuation strategies. It can be seen that the pretension in each cable must progressively increase from tip to root for the SR solution while the pretension is the same in each cable except the tip cell for the MC solution. The bending stiffness of the MC solution increases with the number of cells while the bending stiffness of the SR solution decreases with the number of cells. As shown before, the actuator displacements must increase from the root cell to the tip cell for the MC solution to have the same displacement field as the SR solution with equal actuator displacements for each cell. Both solutions will have identical displacement fields with the same drum angular rotation, if the drum for the MC solution has connection points at different radii for each cell's antagonistic pair. Additionally, the MC solution that employs a drum with varying radii will have the same torque exerted on the actuator – due to internal and external loads – as a structure using a constant radius drum and the SR solution.

The analytical solutions for the remote actuation strategies can also be used to estimate the active structural efficiency, which is a measure of how much work it takes to move the unloaded structure to its maximum displacement, W_{struct} , compared the amount of work to move the loaded structure to its maximum displacement, $W_{struct} + W_e$

$$\eta_s = 1 - \frac{W_{struct}}{W_{struct} + W_e} \quad (18)$$

The work done to move an external tip load, P , a displacement, A , is

$$W_e = \left(NPR \frac{L}{h} \right) \left(\frac{h}{NR} \frac{A}{L} \right) = PA \quad (19)$$

While the work to move the unloaded structure due to pretension reorientation alone is

$$W_{struct} = 2N^3 \left(\frac{PL}{2Nh} \right) \frac{R^2}{L} \left(\frac{h}{NR} \frac{A}{L} \right)^2 = \frac{A}{L} \left(\frac{h}{L} \right) \quad (20)$$

Thus an estimate of the active structural efficiency, which does not include the work done to move the unloaded structure due to induced strain, is

$$\eta_s = 1 - \frac{1}{1 + \frac{L}{A} \left(\frac{L}{h} \right)} \quad (21)$$

The active structural efficiency can be maximized only by lowering the normalized tip displacement to zero, increasing the aspect ratio towards infinity or using the noncircular drum that allows more cable to be released than pulled in Eq. (17) for a given drum rotation. Ideally a high aspect ratio would be the best choice to maximize the structural efficiency, but there will be limits due to bending stiffness criteria, maximum allowed actuator torque, and fabrication limitations.

3. Experimental validation

To validate the analytical and numerical solutions, an experimental tensegrity beam has been fabricated. The tensegrity beam is a 3 cell, class 2 structure utilizing the MC routing strategy. The aspect ratio of the beam is $L/h = 6$ with a length $L = 0.72$ m. The beam's cable members are braided stainless steel cables with a diameter of 4.6×10^{-4} m and the strut members are aluminum bars. The axial stiffness of the struts is 370 times stiffer than the cables satisfying the assumption of rigid struts used in the analytical solutions.

The modulus of elasticity for the braided cable was measured using an Instron tension machine following ASTM standard A931. The strain in the cable was measured using a laser extensometer. The end connectors, attached to the Instron, replicated the cable end conditions in the experimental structure. Based on a cable area of 1.6×10^{-7} m², 5 tests were performed to give a mean modulus of $E = 97 \pm 3$ GPa.

To realize the MC routing scheme on a pin-jointed planar structure, cable elements pass over low-friction pulleys to route through a node. The pulleys are mounted on axles where the struts connect to form a node. The struts are mounted on the axles with ball bearing inserts in between to create frictionless hinge joints. The structure was prestressed to the optimal distribution with a pretension of $T_0^{opt} = 19.6$ N using worm gear tensioners while the structure was hanging with the span in the vertical direction. The tension in the top and bottom cables is measured by strain gauge-based load cells placed in-line.

Tests are performed by mounting the beam in a cantilever orientation (Fig. 12) while prescribed loads are applied at the beam's tip via hanging weights. The vertical displacement of a point at the tip of the structure is recorded optically by a series of images, from which the displacements are calculated by an image cross-correlation program written in MATLAB. The horizontal deflection due to elastic deformation of the bottom pinned base node must also be included in the measurement of the vertical deflection of the tip. This displacement causes an additional vertical tip displacement of the following magnitude

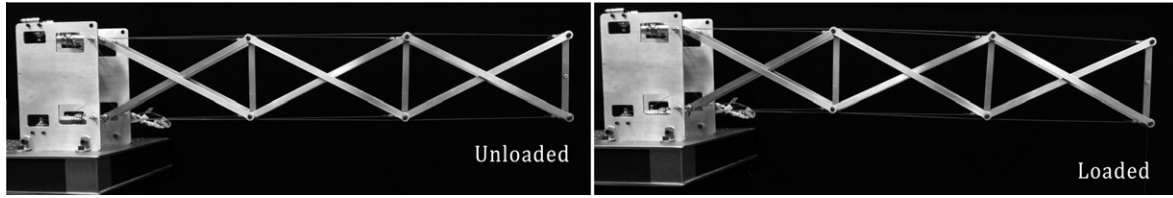


Fig. 12. Experimental tensegrity structure in the loaded and unloaded states. The structure is an MC clustered tensegrity structure with a tip load applied to the free end of the beam.

$$\delta_{tip}^{add} = \delta_{base} \left(\frac{L}{h} \right) \quad (22)$$

The horizontal displacement of the base node, δ_{base} , causes a rigid-body rotation of the beam about the top pinned base node adding to the tip displacement measurement. The displacement of the base node was optically tracked and the load–displacement data is compensated for this effect.

Fig. 13a presents the load–displacement results showing excellent agreement between the analytical, numerical and experimental results. As the tip load increases the structure reaches the critical slackening load, which analytically occurs at a non-dimensional load $P/T_0^{opt} = 1$. The slackening load (defined for the numerical and experimental solutions as the load when any of the cables slacken) for both the experiments and the numerical simulations occurs at a non-dimensional load $P/T_0^{opt} \approx 0.9$. This is due to the self-weight of the structure, which is accounted for in the numerical simulations. The first-order bending stiffness is reported as $K_{bend}^{analytic} = 2217$ N/m, $K_{bend}^{num} = 2221$ N/m and $K_{bend}^{exp} = 2162$ N/m, showing that the experimental results are within 2.6% of the analytical and numerical results. The analytical solution is not valid for the post-critical response, as expected. However, the numerical solution accurately captures the post-critical response of the structure. The post-critical experimental bending stiffness measured is within 2.9% of the numerical bending stiffness, after all of the cables have slackened. The discrepancy between the post-critical experimental response and the numerical response is due to remaining tension in the bottom cables of the first and second cells. The delay in slackening of the first and second cells is due to three-dimensional effects in the experimental setup, explained below with the force density data (Fig. 13b) where the discrepancy is more evident.

Fig. 13b shows the normalized force densities in the top and bottom cables. The force densities are normalized by the nominal

force density in the tip cell, λ_0 . The force densities of the top and bottom cables in the three cells are different due to the non-uniform distribution of tension among the cells and the varying lengths of the cable elements routing to each cell. Moreover, the highest force densities are in the base cell and the lowest are in the tip cell. The force densities of the bottom cables drop with the applied load, while the force densities of the top cables increase. The force densities in the top and bottom cables of a cell do not start at the same value as they would ideally due to self-weight acting as an initial applied load to the structure. Self-weight is compensated for in the analytical solutions by matching the force densities of the numerical solution at the zero applied load value ($P/T_0^{opt} = 0$).

It can be seen that again there is excellent agreement between the analytical, numerical and experimental results. However, there are more obvious discrepancies in the experimental force density data. As discussed previously, the force density in the bottom cable of the tip cell goes slack prior to the first and second cells. Ideally, all of the bottom cables slacken simultaneously when the optimal pretension distribution is applied. The delay in slackening of the first and second cells is due to three-dimensional effects of the experimental structure. The nodes are not perfect hinge joints, due to play in the ball-bearing inserts. Moreover, the fabrication of a two-dimensional structure in three dimensions leads to some load eccentricities at the nodal points. As such when loads are applied to the tip, the beam not only deflects vertically in-plane but also slightly buckles out-of-plane at the interface between the first and second cells. This causes an increase in the tension of the bottom cables of the first and second cells, delaying their slackening and affecting the slope of the force density curve. The tip cell is not significantly affected by the three-dimensional effects and thus the experimental tip cell results track the numerical simulation accurately. Even with the delay in slackening of the first two cells,

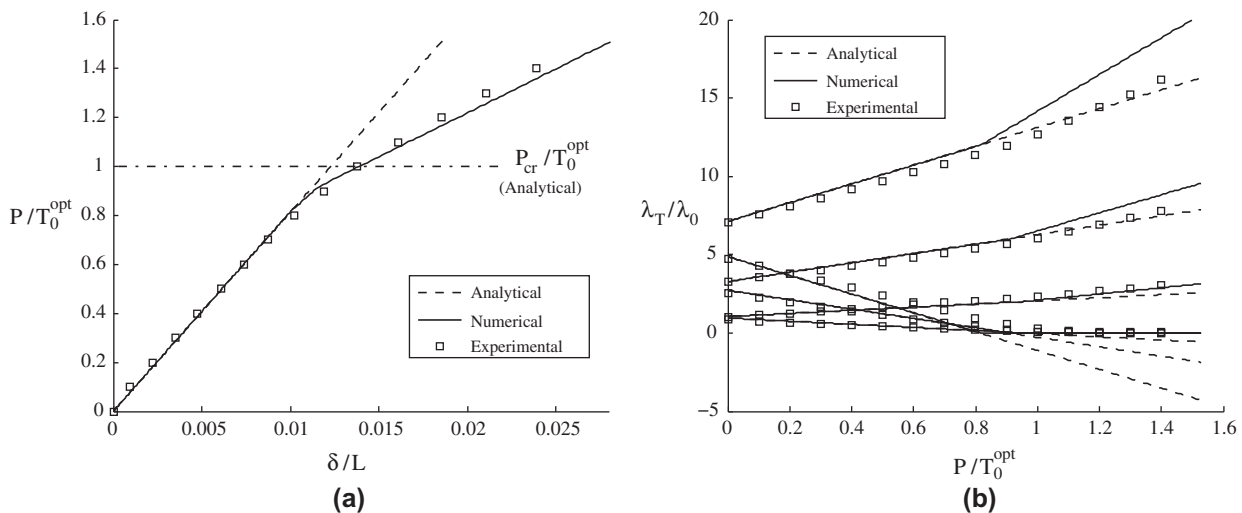


Fig. 13. Comparing the analytical, numerical and experimental results: (a) loading–displacement response and (b) the force density response.

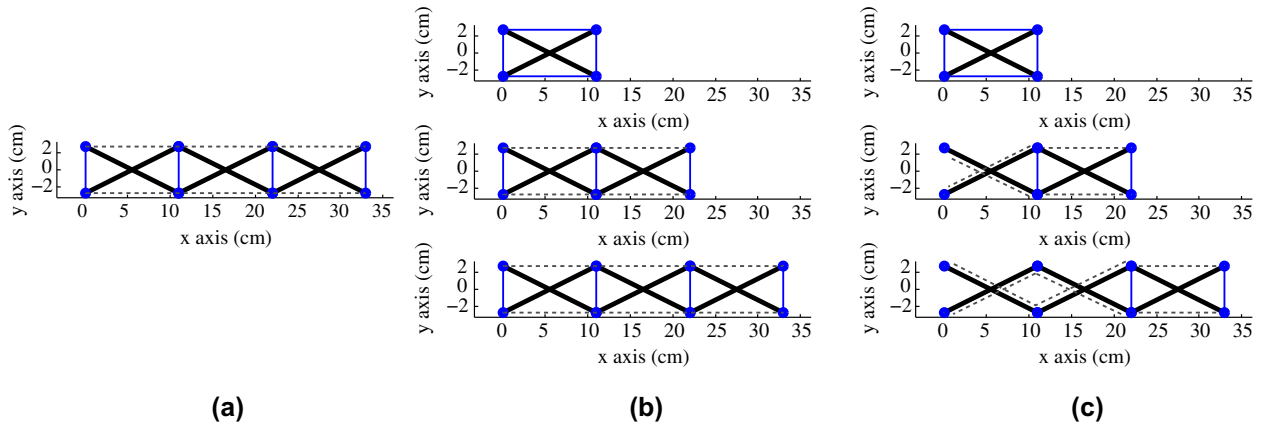


Fig. 14. Prestress modes of (a) the SC structure, (b) the MC structure and (c) the SR structure.

the top cables show a discontinuous increase in tension when the bottom cables of those cells slacken, as predicted by the numerical solutions. Also, as expected, the analytical solution is not valid in the post-critical regime. Load eccentricities can be minimized by fabricating two planar structures with common nodes and cables running between them.

Overall, the experimental results of the MC tensegrity beam show excellent agreement with both the analytical and numerical results validating the assumptions and derivations of these solutions.

4. Optimal routing strategy

In order to reduce the number of necessary actuators, relieve element size constraints due to embedded actuators and move the actuator mass out of the structure, a routing strategy should be employed that connects the active elements of the structure to an actuator that is remotely located. An obvious question to ask is, which remote actuation strategy is the best alternative to embedded actuation?

To answer this question, the analytical solutions as well as the generalized numerical model (Moored and Bart-Smith, 2009) is used. The general tensegrity mechanics formulation will be referred to as clustered tensegrity mechanics, as it allows the grouping of cable elements into *clusters* that route throughout a tensegrity structure. A cluster is a group of individual cable elements in a structure that are combined into one continuous cable element that runs over frictionless pulleys, through frictionless loops or through frictionless holes at the nodes of a structure and can be routed to a remotely located actuator. Cable clusters can be routed through struts, double-back on themselves or even route between the same nodal points as a passive cable.

To be clear, clustered tensegrity mechanics are the mechanics of a tensegrity structure with cable clusters with or without connected actuators. Clustered actuation is *any* actuation strategy where the actuator is connected to a cable cluster. In general, any remote actuation strategy is a clustered actuation strategy. It has been shown that the clustered tensegrity mechanics are a more general form of the classical tensegrity mechanics and thus they will also be utilized to model embedded actuation (in the limit when $\mathbf{S} \equiv \mathbf{I}$) (Moored and Bart-Smith, 2009).

To compare the remote actuation strategies, each of them (SC, MC and SR) must first have a prestress solution to even be a viable routing strategy. As an example, the MC solution must have three cables on the top and bottom of the root cell, two on the middle and one on the tip cell. Then the clustering matrix² can be used

to group the cables generating the proper clustered equilibrium matrix. By determining the nullspace solution of the clustered equilibrium equations and applying the prestress algorithm to find the elementary states (Moored and Bart-Smith, 2009; Quirant et al., 2003; Masic, 2004; Quirant, 2007), the prestress modes are found (Fig. 14). The numerical solutions of the elementary prestress states are shown in Eq. (23)

$$\mathbf{N}^{SC} = \begin{bmatrix} 1 \\ 1 \\ 3 \\ 6 \\ 6 \\ 3 \\ 3 \\ 3 \\ 3 \\ 3 \\ 3 \\ 3 \\ 3 \end{bmatrix}, \quad \mathbf{N}^{MC} = \begin{bmatrix} 1 & 0 & 0 \\ 0 & 1 & 0 \\ 0 & 0 & 1 \\ 1 & 0 & 0 \\ 0 & 1 & 0 \\ 0 & 0 & 1 \\ 1 & 2 & 3 \\ 1 & 4 & 6 \\ 0 & 2 & 6 \\ 0 & 0 & 3 \\ 1 & 2 & 3 \\ 1 & 2 & 3 \\ 0 & 2 & 3 \\ 0 & 2 & 3 \\ 0 & 0 & 3 \\ 0 & 0 & 3 \end{bmatrix}, \quad \mathbf{N}^{SR} = \begin{bmatrix} 1.0 & 0 & 0 \\ 0 & 1.0 & 0 \\ 0 & 0 & 1.0 \\ 1.0 & 0 & 0 \\ 0 & 1.0 & 0 \\ 0 & 0 & 1.0 \\ 1.0 & 0 & 0 \\ 1.0 & 2.12 & 0 \\ 0 & 2.12 & 3.24 \\ 0 & 0 & 3.24 \\ 1.0 & 1.89 & 2.89 \\ 1.0 & 1.89 & 2.89 \\ 0 & 2.12 & 2.89 \\ 0 & 2.12 & 2.89 \\ 0 & 0 & 3.24 \\ 0 & 0 & 3.24 \end{bmatrix} \quad (23)$$

The actual prestress state of the structure can be any positive linear combination of the elementary prestress modes

$$\lambda = \mathbf{N}\alpha \quad (24)$$

The prestress states are sets of force densities having units of N/m. If a specific pretension, T_0 , in a set of cables is desired then a specific α may be applied.

It is interesting to note that when the SC solution is applied to the beam structure, the number of prestress states is reduced to a single state. A single prestress state would greatly simplify the fabrication process and is highly desired. Conversely, the MC and SR solutions each have three prestress states. Since all three routing solutions have a prestress state, then, as of now, they are all viable candidates. Next, the internal mechanisms for the structures are calculated following the procedure outlined in Moored and Bart-Smith (2009). Both the MC and SR structures have no internal mechanisms while the SC structure has two internal mechanisms that can be seen in Fig. 15.

² Defined in Moored and Bart-Smith (2009).

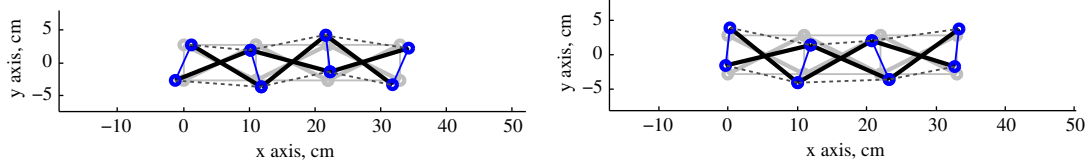


Fig. 15. The SC structure has two internal mechanisms (above) while the MC and SR structures only have rigid-body mechanisms.

Table 2

Eigenvalues of the stiffness matrix for the SC, MC and SR structures, for pretensions of $T_0 = 20$ N and $T_0 = 200$ N. The three rigid-body zero eigenvalues are omitted.

SC: $T_0 = 20$ N	SC: $T_0 = 200$ N	MC: $T_0 = 20$ N	MC: $T_0 = 200$ N	SR: $T_0 = 20$ N	SR: $T_0 = 200$ N
51,859,900	51,854,400	51,948,800	51,940,000	51,950,000	51,943,300
51,834,400	51,834,400	51,855,500	51,856,600	51,881,100	51,878,800
36,474,400	36,472,200	36,594,400	36,592,200	36,602,200	36,599,900
36,420,000	36,422,200	36,461,100	36,464,400	36,425,500	36,424,400
21,215,500	21,216,600	21,238,800	21,239,900	21,308,800	21,308,800
20,953,300	20,954,400	21,006,600	21,009,900	21,017,700	21,018,800
195,577	411,900	186,055	424,811	346,511	348,777
320,200	390,399	223,144	400,155	393,611	398,811
385,311	322,022	355,866	359,699	401,966	411,966
401,966	195,988	391,633	224,133	199,711	207,566
40,532	44,924	403,099	198,599	180,999	181,133
186	1862	30,110	34,204	49,915	52,786
180	1680	12,592	13,445	6110	6445

Even though the SC structure has internal mechanisms they can be stabilized by the prestress in the structure. The stability of the all three solutions must be checked by evaluating the clustered stiffness matrix

$$\mathcal{K} = \mathbf{C}\mathbf{g}\mathbf{l}^{-1}\mathbf{S}^T\mathbf{y}\mathbf{a}\mathbf{l}^{-1}\mathbf{S}\mathbf{l}^{-1}\mathbf{g}^T\mathbf{C}^T + \mathbf{C}\hat{\mathbf{g}}_1\mathbf{M} - \mathbf{C}\mathbf{g}\mathbf{l}^{-1}\left(\hat{\lambda}_1^* - \mathbf{S}^T\hat{\lambda}_1\mathbf{S}\right)\mathbf{l}^{-1}\mathbf{g}^T\mathbf{M} \quad (25)$$

If there are no internal mechanisms and the eigenvalues of the stiffness matrix are positive then a structure is stable and is first-order rigid (Connelly and Whiteley, 1996). If there are internal mechanisms and the eigenvalues of the stiffness matrix are positive, only when there is prestress present, then a structure is stable and is prestress stabilized. The eigenvalues of the stiffness matrix for the three structures are shown (without the zero rigid-body mechanisms) for two different levels of pretension (Table 2). The pretension is applied to the top and bottom cables of the different structures.

All three routing strategies produce structures that are stable, however the SC solution is prestress stabilized while the MC and SR solutions are first-order rigid. It can be seen that the lowest eigenvalues of the SC solution (which correspond to the internal mechanisms, since they go to zero as the prestress goes to zero) are orders of magnitude lower than the lowest eigenvalues of the MC and SR solutions. It is also noted that the lowest eigenvalues of the SC solution are proportional to the amount of pretension in the structure, whereas for the MC and SR solutions there is only a slight increase in the eigenvalues due to an order of magnitude increase in the pretension. For all three of these structures the relative stiffness, k_r , is between 100 and 1000, meaning that the material properties dominate the bending stiffness response by a factor of 100–1000 as long as no internal mechanisms are present and thus the pretension will not have a large effect on the bending stiffness of the first-order rigid structures. Consider also that to stiffen the mechanisms of the SC structure such that the bending stiffness is comparable to the MC and SR structures, a pretension on the order of 1 kN must be applied. This extreme amount of pretension is impractical. For a more reasonable range of pretension (on the order of 10 N) the SC solution undergoes large deformations with small applied loads.

To highlight this point, a three cell SC beam with the following parameters ($L/h = 6$, $L = 0.33$ m, $E = 111$ GPa, $A_c = 1.4 \times 10^{-7}$ m², $T_0 = 5$ N) has been numerically simulated (Fig. 16a) with an applied tip load of $P = 7$ N and compared to an experimental structure (Fig. 16b).

When a 7 N tip load is applied to this structure it has a normalized tip displacement of $A/L = 38.9\%$. The first-order bending stiffness is 2.85 N/m. With this bending stiffness and an applied tip load of 7 N, a normalized tip displacement of 744% would be predicted, however the loading response is highly nonlinear. The first-order bending stiffness is dominated by the geometry and the pretension, not the material properties. This is characteristic of prestress stabilized structures (Pellegrino, 1990). Also, note that the structural deformation has the same modeshape as the internal mechanism found in Fig. 15a. After the structure begins to displace away from the neutral position, strain is induced in the structure and the material properties play a greater role to limit the displacement. Nonetheless, it takes a pretension of 6.7 kN to give this structure a first-order bending stiffness of 2121 N/m which limits the normalized tip displacement to 1% under a 7 N tip load. It was found that using the SC solution routed along the exterior of a structure produced a weakly prestress stabilized structure even for three-dimensional structures. Thus, the SC solution is not recommended for load bearing applications.

Now that the SC solution is no longer a viable candidate, how do the MC and SR solutions compare? Which solution is optimal for the application of an artificial pectoral fin? Ideally, using a quasi-static design approach, a tensegrity-based pectoral fin should not deform much under hydrodynamic loads. For an open-loop strategy to be employed, the structures should be stiff enough to support the external loads without significantly deviating from the prescribed kinematics. This leads to a comparison of the MC and SR solutions based on their stiffness-to-mass ratio, \mathcal{K}_{bend}/M . Moreover, the optimal amount of material used to fabricate a tensegrity structure with the two strategies applied should be compared when the failure load for the structures is held constant. This leads to a second comparison based on the strength-to-mass ratio, P_{fail}/M .

Appropriate conditions need to be applied to both structures such that they are comparable. The first condition, is that the aspect ratio, beam span length, and material properties are the same.

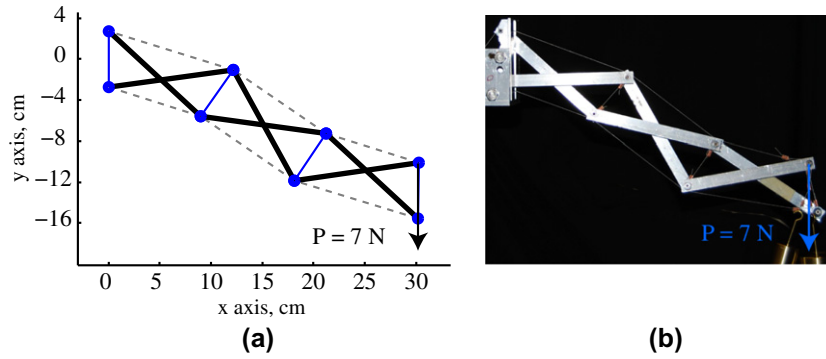


Fig. 16. The SC structure has $T_0 = 5$ N in the top and bottom cables and a 7 N tip load applied to the structure. The structure has a normalized tip displacement of $A/L = 38.9\%$.

The second condition, is there must be just enough pretension in the structures such that no cable slackening occurs under a 5 N tip load. The third condition, is that the structure's mass must be minimal under the pretension loads and under the 5 N tip load applied either upward or downward. Lastly, after these three conditions are met the first-order bending stiffness and the optimal mass of the structure are measured and then compared. The first-order bending stiffness can either be measured using the clustered stiffness matrix (Eq. (25)) or an infinitesimally small tip load can be applied to the structure and the tip displacement can be measured ($K_{bend} = \Delta P / \Delta z$).

The first condition is straightforward and easily met. An aspect ratio $L/h = 8$, span length $L = 0.33$ m, a modulus of elasticity for the cables of $E = 97$ GPa (braided stainless steel cable, Section 3) and a modulus of elasticity for struts of $E_s = 69$ GPa (aluminum) are chosen.

For the second condition, the optimal amount of pretension that a structure must have such that no cables go slack under a tip load can be found from the analytical solutions derived in Section 2. The optimal pretension solution for the SR beams is $T_0 = [(2N - 1), \dots, (2N - 2j + 1), \dots, 3, 1]T_0^{opt}$ and $T_0 = [2, 2, 2, \dots, 1]T_0^{opt}$ for the MC beam.

To satisfy the third condition the two structures must be mass minimized for the pretension loads first and then for the tip load. For the structure to have minimal mass, all of the elements should simultaneously be on the cusp of failure under a given load. This ensures that there is no unnecessary material in the structure. Since the cables can only be in tension they will fail when the stress in the element reaches the yield stress of the material ($\sigma_y = \bar{\lambda}_i \bar{l}_i / \bar{a}_i$ where $\sigma_y = 210$ MPa for stainless steel³). If the radius of the cable is shrunk until the stress in the cable reaches the yield stress, then the cable will have minimal mass. The minimum radius and minimum mass of each cable can be calculated by the following:

$$r_c = \sqrt{\frac{\bar{\lambda} l}{\pi \sigma_y}} \quad \text{and} \quad m_c = \rho_c \pi l_0 r_c^2 \quad (26)$$

The density, ρ_c , of stainless steel is 8000 kg/m³. The struts in a tensegrity structure are almost always in compression and thereby will fail by Euler buckling as long as their slenderness ratio is high enough. The radius of a strut (assuming a solid circular cross-section) can be shrunk such that the force in the strut reaches the critical Euler buckling load, $P_{euler} = E_s \pi^3 r_s^4 / 4 l_0^2$. When this radius is reached the minimal strut radius and minimal strut mass are defined

$$r_s = \left(\frac{4 \bar{\lambda} l_0^2}{E_s \pi^3} \right)^{1/4} \quad \text{and} \quad m_s = \rho_s \pi l_0 r_s^2 \quad (27)$$

³ Notation is from Moored and Bart-Smith (2009).

The density, ρ_s , of aluminum is 2700 kg/m³ and the modulus of elasticity, E_s , is 69 GPa. Once the first three conditions are met, the two routing strategies can be compared. Fig. 17 shows how the stiffness-to-mass and strength-to-mass ratios of the two strategies compare. It can be seen that the MC strategy has a higher stiffness-to-mass and strength-to-mass ratio at all values of $N > 1$ that were used in the calculations. By looking at Table 3, the increased stiffness-to-mass ratio comes from both lower mass and higher stiffness of the MC solution. The SR solution cannot match the performance of the MC solution since the routed cable that clusters over the struts plays no role in the bending stiffness of the structure while the added cable length lowers the element stiffnesses to create a softening effect. Furthermore, if the forces in the members are inspected, it can be seen (under the three normalizing conditions) that the forces in the struts of the SR solution are actually higher than the MC solution, necessitating the use of thicker, more massive struts, to avoid buckling. This effect is reflected in the higher mass of the SR solution (Table 3) compared to the MC solution and leads directly to the results that the MC solution always has a higher strength-to-mass ratio when $N > 1$. It is interesting to note that for both strategies there is an optimal number of cells to maximize the stiffness-to-mass: $N = 6$ for the MC solution and $N = 2$ for the SR solution. The strength-to-mass ratio is optimal at $N = 6$ for the MC solution and $N = 4$ for the SR solution. Fascinatingly, the MC solution is optimal in stiffness-to-mass and strength-to-mass at the same number of cells, $N = 6$. Furthermore, Fig. 17 this shows that finite, instead of infinite, complexity is optimal as was previously found (Skelton and de Oliveira, 2009).

5. Design example

Using the analytical solutions, a tensegrity-based artificial pectoral fin can now be designed. At this point, a target displacement field needs to be defined. A new analytic kinematic model that describes the motions of manta ray pectoral fins will be utilized (Moored, 2010; Moored et al., in preparation). This kinematic model describes the deformations of the neutral plane of a ray-like fin throughout a flapping cycle. The model uses four fitting parameters which are tuned to an individual species of the batoid family. The parameters have been determined for the Atlantic stingray, the cownose ray and the manta ray. The kinematic model tuned to the manta ray will be used for this study.

Consider a series of four tensegrity beam structures composing the internal structure of an artificial pectoral fin (Fig. 18). The fin provides a surface with which the underlying structures can interact and apply forces to the fluid environment. This boundary between the structures and the fluid could be an elastomer skin or a sliding plate scale-like solution, but for now this will be neglected. If the fin has a trapezoidal planform shape, similar to the

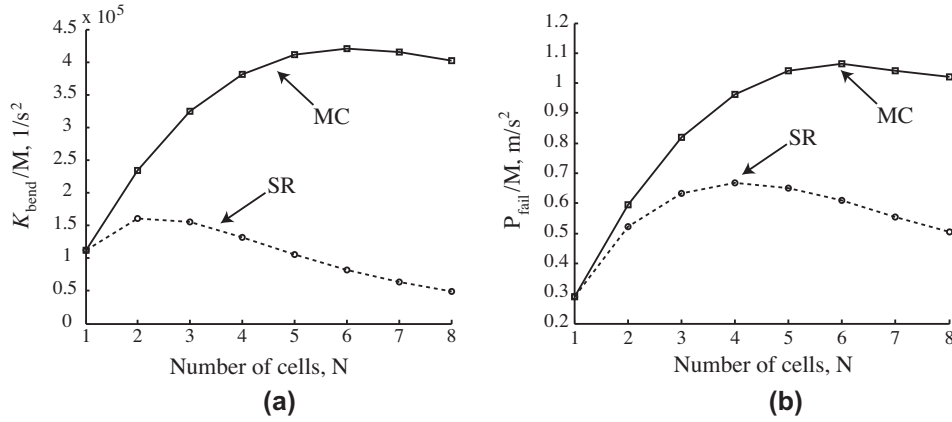


Fig. 17. Stiffness-to-mass ratio of the optimized structures with one using an SR strategy while the other uses a MC strategy.

Table 3

Minimum structural mass and bending stiffness of clustered structures using the MC and SR strategies, subjected to pretension loads and a 5 N tip load. The number of cells, N , in the structure varies while the overall beam aspect ratio L/h is held constant.

N	M^{MC} (g)	M^{SR} (g)	κ_{bend}^{MC} (N/m)	κ_{bend}^{SR} (N/m)
1	17.3	17.3	1940	1940
2	8.4	9.6	1965	1546
3	6.1	7.9	1975	1224
4	5.2	7.5	1980	989
5	4.8	7.7	1982	812
6	4.7	8.2	1984	676
7	4.8	9	1984	569
8	4.9	9.9	1985	483

planform shape of myliobatoid rays, and it is oscillating in water at about 1.5 Hz, the normal forces on the fin can be estimated by calculating the drag on a square flat plate moving through water normal to its surface. The drag force on a plate in this configuration will have a drag coefficient, $c_D \approx 1.17$ and can be calculated from

$$F_D = \frac{1}{2} c_D \rho S U_f^2 \quad (28)$$

The area of the plate is S , the density of water is ρ and the velocity of the plate relative to the fluid is U_f . However, the case of a root-fixed flapping fin is different than a flat plate moving through a fluid. As a simple estimate, the force on the fin will be calculated similarly except the velocity will be assumed to vary from the root of the fin to the tip. Furthermore, the fin chord changes as a function of the span. Thus, considering these differences a simple estimate of the normal force on an artificial pectoral fin is the following:

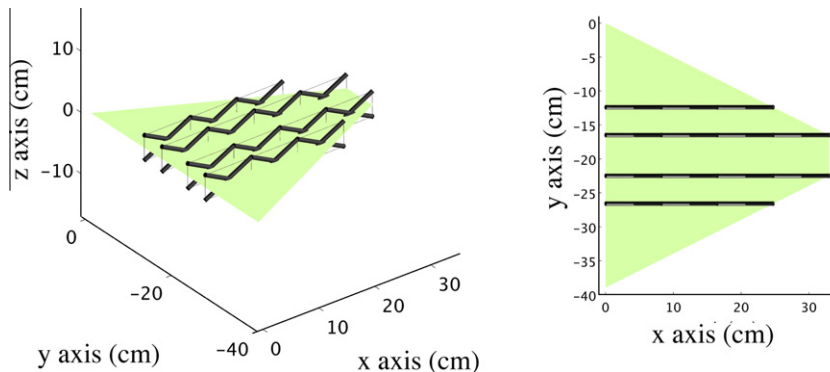


Fig. 18. Four MC tensegrity beam structures compose the structural foundation of an artificial pectoral fin.

$$F_L = \frac{1}{2} c_D \rho \int_0^L c(x) U_f(x)_{max}^2 dx \quad (29)$$

The chord length as a function of the span position is $c(y)$. Using an analytical kinematic model matched to the manta ray as a target deformation field, the maximum velocity distribution along the span of a fin is determined

$$U_f(x)_{max} = \frac{2\pi f m}{L} x^2 \quad (30)$$

The frequency of flapping is f while m is the amplitude fitting parameter determined for a given species (Moored, 2010). Furthermore, for a trapezoidal fin the chord length varies with the span as $c(y) = c_{root} + (c_{tip} - c_{root})y/L$, where the root chord length is c_{root} and the tip chord length is c_{tip} . Using this chord function and the velocity distribution (Eq. (30)) the integral (Eq. (29)) for the lift estimate can be solved

$$F_L = \frac{1}{3} c_D \rho \pi^2 f^2 m^2 L^3 (c_{root}/5 + c_{tip}) \quad (31)$$

This gives a design estimate of the amount of loading to be expected on the underlying structure. Using a density of $\rho = 1000 \text{ kg/m}^3$, a frequency of $f = 1.5 \text{ Hz}$, an amplitude parameter of $m = 0.48$, a span length of $L = 0.33 \text{ m}$, a root chord length or $c_{root} = 0.33 \text{ m}$, and a tip chord length of $c_{tip} = 0.06 \text{ m}$ a total lift load on the fin of approximately 9 N is calculated. To be conservative it will be assumed that half of the total load is applied to each beam as a tip load ($P = 5 \text{ N}$ for each beam).

The MC solution has been shown to provide optimal structural performance, so this strategy will be employed in the design. The fin will be composed of four beams that will be symmetric about the mid-chord position (Fig. 18). The two inner beams will be composed of four cells to maximize the shape resolution in the span

direction under fabrication limitations. The two outer will be composed of three cells to fit the trapezoidal planform shape. To directly drive the drum with an actuator, thereby eliminating the need for a gearing system and making a more compact design that avoids gear backlash, the aspect ratio can be set based on the maximum allowable actuator torque

$$\frac{L}{h} = \frac{\tau_a^{max} - NPR \frac{A}{L}}{NPR} \quad (32)$$

If, for instance, the maximum allowable torque is 3.4 N m (Hitec Servo HS-7950TH), N is 4, the minimum drum radius, R , due to fabrication constraints of the pretensioning mechanisms is 0.02 m and the non-dimensional tip amplitude is 0.44, then the aspect ratio is approximately 8. To keep the cell aspect ratio the same for the outer beams they will have a beam aspect ratio of 6. Moreover, the inner beams will have a span length of $L = 0.33$ m while the outer beams will have a span length of $L = 0.2475$ m giving both beams the same thickness of $h = 0.04$ m.

First, the pretension throughout the structure is set to the optimal value that keeps cables from going slack. This keeps the bending stiffness maximized and keeps the motion smooth without structural instability, while minimizing the amount of strain energy stored in the structure. Using the analytical equations, described in Table 1, the optimal pretension is calculated to be $T_0^{opt} = 5$ N for both the three-cell and four-cell beams. Thus, the pretension for the top and bottom cables is the following:

$$T_0 = [10, 10, 5]^T \text{ N} \quad (3 \text{ cells}) \quad \text{and} \\ T_0 = [10, 10, 10, 5]^T \text{ N} \quad (4 \text{ cells}) \quad (33)$$

To create an artificial pectoral fin that mimics the motions of the manta ray, the kinematics of the artificial structure should match the kinematics of the manta ray. Given the kinematic model of the manta ray (Moored, 2010), the underlying structures should be stiff enough to not significantly deviate from the prescribed kinematics when under load. As a design criteria, the structure should not deform more than 1% of the span length under the max load. This stiffness criteria is used such that the tensegrity-supported region of a fin has good power transfer to the surrounding fluid at a range of flapping frequencies, however, tip and trailing edge compliance can be added when the structure is encapsulated in a synthetic skin. The maximum load occurs when the fin passes through the neutral position as this is where the highest velocity is attained (quasi-static assumption). Thus, given the maximum load and deflection criteria, the necessary bending stiffness can be calculated

$$\mathcal{K}_{bend} = \frac{P_{max}}{0.01L} \quad (34)$$

For the three-cell beam $\mathcal{K}_{bend} \geq 2020$ N/m and for the four-cell beam $\mathcal{K}_{bend} \geq 1515$ N/m. The bending stiffness equation (Table 1) can be rearranged to calculate the necessary cable area to achieve a given bending stiffness. The pretension contribution can be neglected in this case ($k_r \gg 1$) and the area can be written in terms of the diameter of the cable

$$D_c = \frac{10L}{Nh} \sqrt{\frac{2(2N-1)P_{max}}{\pi E}} \quad (35)$$

$E = 97$ GPa is used for the modulus of elasticity for the braided stainless steel wire rope. A cable diameter of $D_c = 0.26$ mm is calculated for the three-cell beam and $D_c = 0.3$ mm is calculated for the four-cell beam. Comparable diameter braided stainless steel wire rope has a breaking strength of approximately 111 N. Thus, with a factor of safety, a reasonable failure criteria for this cable is when the force in the cable reaches half of the breaking strength ($F_{fail} = 55.5$ N) as the cable remains linear elastic up to 90 N (Houle, 2009).

Next, the actuator stroke must be calculated to achieve a desired displacement field for each beam. The x coordinates for the neutral axis of the three-cell beams in the undeformed (flat) configuration are $x_f = [0, 0.0825, 0.165, 0.2475]^T$ while the coordinates for the four-cell beams are $x_f = [0, 0.0825, 0.165, 0.2475, 0.33]^T$. The change in vertical displacement of each cell can then be calculated from the kinematic model

$$\frac{\Delta A}{L} = [0.03, 0.09, 0.14]^T \quad (3 \text{ cells}), \\ \frac{\Delta A}{L} = [0.03, 0.09, 0.14, 0.19]^T \quad (4 \text{ cells}) \quad (36)$$

The actuator strokes can be calculated (Table 1) using the change in vertical displacement (Eq. (36))

$$\frac{\delta_a}{h} = [0.12, 0.24, 0.36]^T \quad (3 \text{ cells}), \\ \frac{\delta_a}{h} = [0.12, 0.24, 0.36, 0.48]^T \quad (4 \text{ cells}) \quad (37)$$

The drum radii necessary to achieve the target displacement field for an actuator rotation ($\theta_a = \delta_a^1/R$) are $r = R[1, 2, 3]^T$ and $r = R[1, 2, 3, 4]^T$ for a three and four-cell beam, respectively. Thus the actuator rotation necessary (Table 1) is the following:

$$\theta_a^{max} = 0.24 \text{ rad} \quad (\text{exact case}), \\ \theta_a^{max} \approx 0.22 \text{ rad} \quad (\text{approximate case}) \quad (38)$$

Given the maximum actuator stroke and the oscillation frequency, the peak and average velocity of the actuator can be calculated

$$\dot{\theta}_a^{max} = 2\pi f \theta_a^{max} \quad (\text{peak}), \quad \dot{\theta}_a^{avg} = 4f \theta_a^{max} \quad (\text{average}) \quad (39)$$

Thus the peak actuator velocity is 2.26 rad/s and the average actuator velocity is 1.44 rad/s. The drum radii, maximum actuator stroke and maximum actuator velocity are all set such that the artificial beam structures closely match the biological displacement field in bending. Furthermore, the torque to actuate an unloaded structure, $\tau_{a,i}$, due to pretension reorientation can be directly calculated

$$\tau_{a,i}^{max} = 0.111 \text{ N m} \quad (3 \text{ cells}), \quad \tau_{a,i}^{max} = 0.196 \text{ N m} \quad (4 \text{ cells}) \quad (40)$$

The torque on the actuator due to a tip load is calculated

$$\tau_{a,e}^{max} = 1.86 \text{ N m} \quad (3 \text{ cells}), \quad \tau_{a,e}^{max} = 3.3 \text{ N m} \quad (4 \text{ cells}) \quad (41)$$

It can be seen, in this case, that the torque due to pretension reorientation is not very significant compared to the torque due to external loads on the structure. The average torque due to an oscillating tip load and an oscillating unloaded structure can also be calculated

$$\tau_{a,e}^{avg} = \frac{2\tau_{a,e}^{max}}{\pi} \quad \text{and} \quad \tau_{a,i}^{avg} = \frac{2\tau_{a,i}^{max}}{\pi} \quad (42) \\ \tau_a^{avg} = \tau_{a,e}^{avg} + \tau_{a,i}^{avg}$$

Thus the average torque for the three cell beams is 1.3 N m and the average torque for the four cell beams is 2.2 N m. Moreover, the peak power consumption and the average power consumption of the actuators can be calculated

$$P_{max} = \tau_{a,e}^{max} \dot{\theta}_a^{max} \quad (\text{peak}), \quad P_{avg} = \tau_a^{avg} \dot{\theta}_a^{avg} \quad (\text{average}) \quad (43)$$

The peak power consumption for the three and four cell beams respectively is 4.2 W and 7.5 W, while the average power consumptions are respectively 1.9 W and 3.2 W. The total average power consumption of all four beams is 10.2 W. The active structural effi-

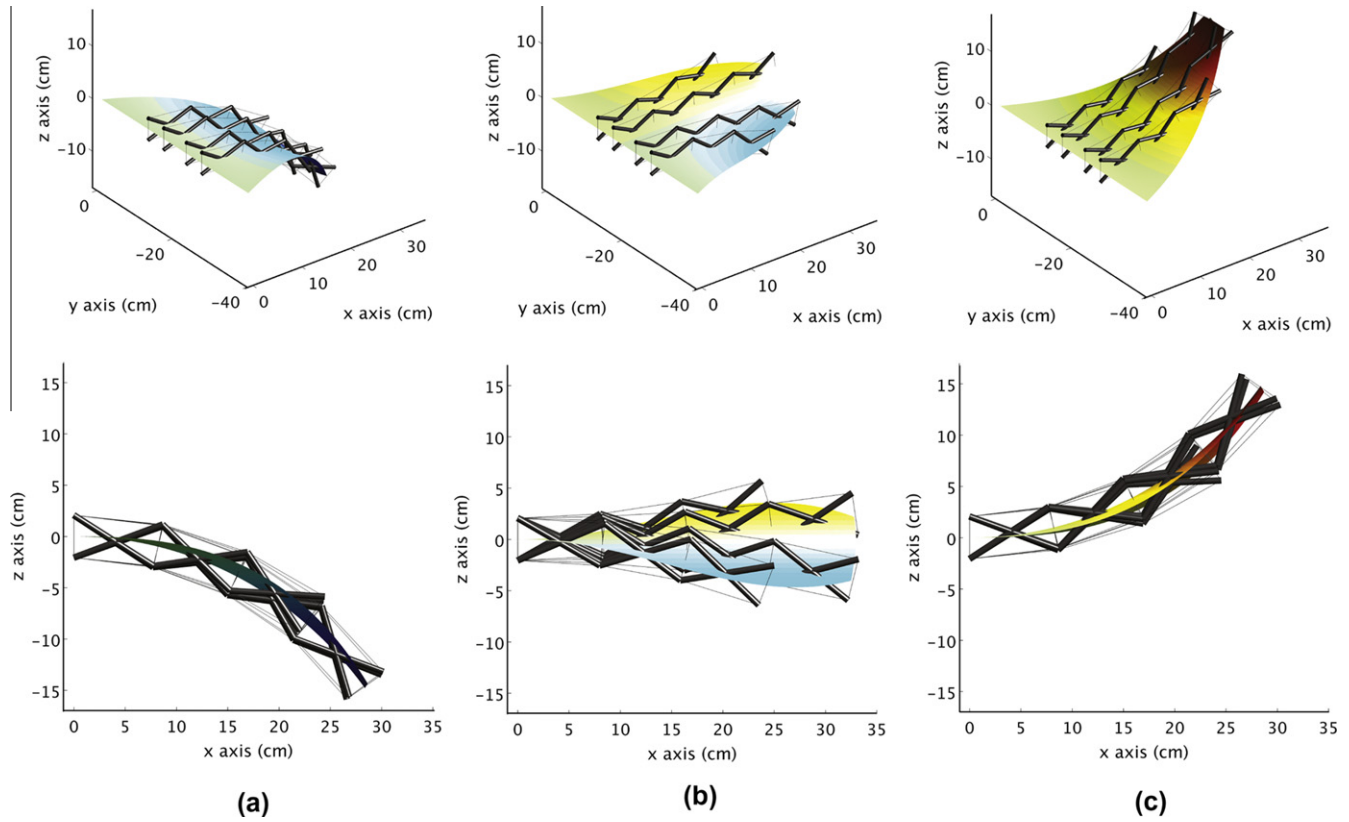


Fig. 19. The proposed artificial pectoral fin is shown (four tensegrity beam structures) at different time steps during a flapping cycle under the simple hydrodynamic loads. The trapezoidal surface represents the kinematic model that describes the pectoral fin deformations of the manta ray. It can be seen that the tensegrity-based fin can closely match the prescribed motion with open-loop actuation. (a) Shows the maximum downward deflection, (b) shows the fin passing through the mid-plane and (c) shows the maximum upward deflection.

ciency can be estimated as the average of the active structural efficiencies for each beam structure (Eq. (21)) where $A/L = 0.35$ and 0.44 for the three and four cell beams, respectively. Thus the active structural efficiency for the fin structure is approximately 95%.

The torque, stroke, velocity and power calculations allow for appropriate actuator selection and determining the open-loop actuation waveform. Using these analytical equations is the first step to designing an active tensegrity fin structure. From the equations, it is clear how a variation in the parameters will vary the performance of the active beam structures without having to carry out an exhaustive parametric study. The design equations can be used to hone in on a set of parameters that can be applied to full numerical analysis for final confirmation of the performance and to investigate the structural elements for failure.

The numerical model is now used to analyze the tensegrity-based artificial pectoral fin proposed above. The analysis is a quasi-static analysis over a flapping cycle of the fin. The phase delay between the beams is set to match the nondimensional wavenumber utilized by the manta ray, which can be directly calculated from the kinematic model developed to describe ray locomotion, where the phase, $\phi^i = Ky_f^i/L$, where $i = 1 \rightarrow N_{beams}$, (Moored, 2010; Moored et al., in preparation). The manta ray exhibits a non-dimensional wavenumber $K = 2.23$. The y coordinates of the beams are $y_f = [-0.124, -0.165, -0.225, -0.266]^T$ m giving phase delays of $\phi = [-0.8379, -1.1143, -1.5198, -1.7962]^T$ rad. The loading on the beam structure will be assumed to be a cosine function with a maximum magnitude of 5 N acting at the tip of each beam

$$P^i(t) = 5 \cos(\omega t + \phi^i) \quad (44)$$

The actuation for the three and four-cell beams will be assumed to be sine functions with a maximum drum rotation of $\theta_a^{max} = 0.24$ rad

$$\theta_a^i = \theta_a^{max} \sin(\omega t + \phi^i) \quad (45)$$

Fig. 19 shows the tensegrity-based artificial pectoral fin actuating under load with the prescribed motion. The trapezoidal surface is the kinematic model that matches the fin motion of the manta ray. The discrepancy between the prescribed motion and the actual motion of the tensegrity-based fin is quantified as the maximum displacement error of the neutral plane nodal point positions⁴ and the kinematic model. The maximum error for the unloaded fin is 0.75% while the maximum error for the loaded fin is 0.96%. Thus, the analytical stroke and bending stiffness predictions were accurately modeled.

The torque on the four actuators for the unloaded fin can be seen in Fig. 20a, while the torque on the actuators for the loaded fin is shown in Fig. 20b, over a flapping cycle. The maximum torque for the loaded three and four cell beams is calculated to be 1.86 N m and 3.3 N m, respectively, and matches the analytical predictions perfectly. The peak torque on the actuator due to the resistance of the structure is 0.31 N m for the three cell beam and 0.5 N m for the four cell beam. The discrepancy between the analytical prediction and the numerical prediction is due to strain induced in the structure during actuation.

Fig. 21a shows the forces in the elements of the first beam over a flapping cycle and Fig. 21b shows the forces in the second beam.

⁴ Defined as the average position between a top and bottom nodal points at a given span position, x_f .

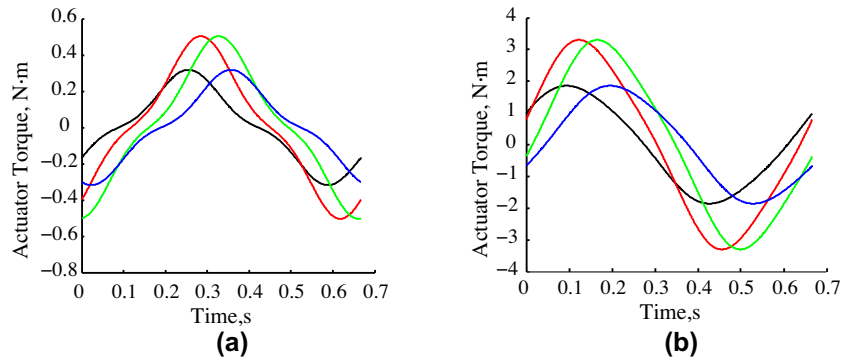


Fig. 20. The actuator torques over one flapping cycle for beams 1 (black), 2 (red), 3 (green) and 4 (blue) are shown. (a) Shows the actuator torques of the unloaded beams, while (b) shows the actuator torques for the loaded beams. (For interpretation of the references to color in this figure legend, the reader is referred to the web version of this article.)

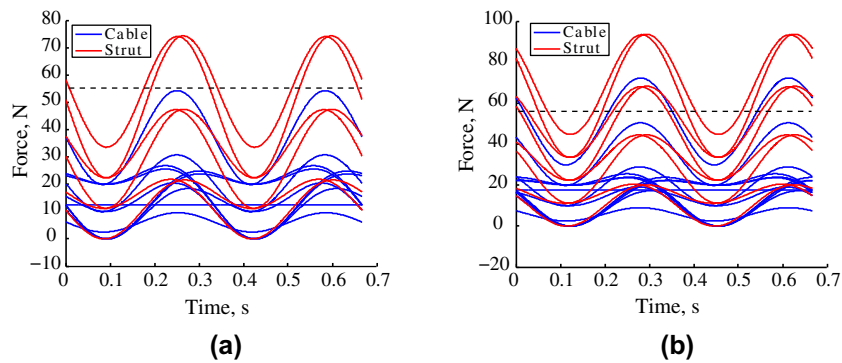


Fig. 21. The forces in the cable elements (blue) and the strut elements (red) are shown when the beams have external loads applied. (a) Shows the forces in the first beam while (b) shows the forces in the second beam. (For interpretation of the references to color in this figure legend, the reader is referred to the web version of this article.)

The cable elements are in blue while the strut elements are in red. The dotted line denotes the failure criteria for the cables stated earlier. It can be seen that one of the cables exceeds the failure criteria. Wire rope with a higher breaking strength (larger diameter) must be used for the vertical cables to avoid failure in the structure. The largest forces occur when the beam structure passes through the neutral plane and the external loads are maximized. Also, note that the top/bottom cables just go slack at the maximum load as predicted analytically.

Lastly, Fig. 22a shows the power consumption over a flapping cycle for the unloaded structure while Fig. 22b shows the power consumption for the loaded fin structure. For the unloaded case,

the maximum power consumption of the three cell beams is 0.27 W and 0.44 W for the four cell beams. The average power consumption is 0.16 W and 0.26 W for the three and four cell beams, respectively. The total average power consumption for the unloaded fin of 0.825 W. For the loaded case, the maximum power consumption of each beam structure is 4.2 W for the three cell beams and 7.5 W for the four cell beams which exactly match the analytical predictions. The average power consumption is 2.1 W and 3.6 W for the three and four cell beams respectively making the analytical predictions 19% and 11% off of the exact values. The total average power consumption for the loaded fin, neglecting the contribution from a skin, is 11.25 W making the

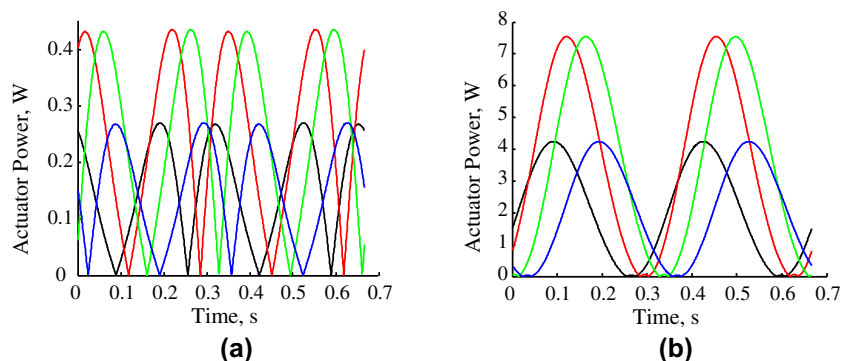


Fig. 22. The power consumption of the actuator for beams 1 (black), 2 (red), 3 (green) and 4 (blue) are shown. (a) Shows the unloaded power consumptions while (b) shows the loaded power consumptions. (For interpretation of the references to color in this figure legend, the reader is referred to the web version of this article.)

analytical prediction off by 9%. The active structural efficiency calculated as $\eta_s = 1 - \mathcal{P}_{avg}^{UL}/\mathcal{P}_{avg}^L$ is 93% making the analytical prediction 2% higher than the exact value. The average power consumption of the unloaded fin is \mathcal{P}_{avg}^{UL} while \mathcal{P}_{avg}^L is the average power consumption of the loaded fin.

6. Conclusions

Three remote routing strategies were developed, modeled and compared. Analytical predictions for an active tensegrity beam utilizing embedded actuation were derived. These predictions describe the actuator displacements necessary to reach a target displacement field, the forces in the active elements due to external loading, the critical slackening load for the cable elements due to tip load, the optimal pretension distribution to keep all cables in tension under a tip load, the first-order bending stiffness of a tensegrity beam, and the forces in active elements during actuation due to the reorientation of pretension. All of the predictions are generalized for any number or cells. The analytical predictions for the embedded actuation tensegrity beams were modified for both the multiple cable-routed (MC) and strut-routed (SR) actuation strategies. The analytical and numerical solutions were shown to have excellent agreement with experimental measurements. The single-cable actuation (SC) strategy was found to produce a prestress stabilized structure that is very compliant and not recommended for load bearing applications. The MC strategy was found to have a higher stiffness-to-mass and strength-to-mass ratio than the SR strategy, making it the optimal remote actuation strategy. Lastly, the utility of the analytical predictions was shown in an example design of a tensegrity-based artificial pectoral fin. Structural performance metrics were calculated showing that the fin structure can closely match the kinematics of the manta ray, under external loading, using open-loop actuation of four actuators remotely located outside of the active structure. This approach costs minimal power consumption and shows the simple design of a high performance tensegrity-based artificial pectoral fin. Although an artificial pectoral fin was the focus application of this article, the findings and design equations are useful for active/deployable space structures, adaptive architecture, robotic manipulators, cell biology and morphing aircraft wings.

Acknowledgements

The authors would like to thank Russell Biagi for his help with the experimental measurements. The authors would like to acknowledge funding from the Office of Naval Research through the MURI program on Biologically-Inspired Autonomous Sea Vehicles (Contract No. N00014-08-1-0642), the David and Lucille Packard Foundation, the National Science Foundation (Contract No. CMS-0384884), and the Virginia Space Grant Consortium.

References

Adam, B., Smith, I., et al., 2007. Self-diagnosis and self-repair of an active tensegrity structure. *Journal of Structural Engineering* 133, 1752.
 Connelly, R., Whiteley, W., 1996. Second-order rigidity and prestress stability for tensegrity frameworks. *SIAM Journal on Discrete Mathematics* 9, 453–491.
 de Jager, B., Skelton, R.E., 2006. Stiffness of planar tensegrity truss topologies. *International Journal of Solids and Structures* 43 (5), 1308–1330.

Djouadi, S., Motro, R., Pons, J.S., Crosnier, B., 1998. Active control of tensegrity systems. *Journal of Aerospace Engineering* 11 (2), 37–44.
 Domer, B., Smith, I., et al., 2005. An active structure that learns. *Journal of Computing in Civil Engineering* 19, 16.
 Fest, E., Shea, K., Domer, B., 2003. Adjustable tensegrity structures. *Journal of Structural Engineering* 129, 515.
 Fest, E., Shea, K., Smith, I.F.C., 2004. Active tensegrity structure. *Journal of Structural Engineering* 130, 1454.
 Furuya, H., 1992. Concept of deployable tensegrity structures in space applications. *International Journal of Space Structures* 7 (2), 143–151.
 Houle, N.E., December 2009. Design, manufacturing and experimental validation of class 2 tensegrity structures for application in a bio-inspired flapping wing. Master's Thesis. University of Virginia.
 Kwan, A., Pellegrino, S., 1994. Matrix formulation of macro-elements for deployable structures. *Computers & structures* 50 (2), 237–254.
 Kwan, A., You, Z., Pellegrino, S., 1993. Active and passive cable elements in deployable/retractable masts. *International Journal of Space Structures* 8 (1–2), 29–40.
 Masic, M., 2004. Design, optimization, and control of tensegrity structures. Ph.D. Dissertation. University of California, San Diego.
 Masic, M., Skelton, R., 2005. Path planning and open-loop shape control of modular tensegrity structures. *Journal of Guidance, Control and Dynamics* 28, 421–430.
 Masic, M., Skelton, R.E., Gill, P.E., 2005. Algebraic tensegrity form-finding. *International Journal of Solids and Structures* 42 (16–17), 4833–4858.
 Masic, M., Skelton, R.E., Gill, P.E., 2006. Optimization of tensegrity structures. *International Journal of Solids and Structures* 43 (16), 4687–4703.
 Moored, K.W., August 2010. The design of a novel tensegrity-based synthetic pectoral fin for bio-inspired propulsion. Ph.D. Thesis. University of Virginia.
 Moored, K.W., Bart-Smith, H., 2007. The analysis of tensegrity structures for the design of a morphing wing. *Journal of Applied Mechanics* 74, 668–676.
 Moored, K.W., Bart-Smith, H., 2009. Investigation of clustered actuation in tensegrity structures. *International Journal of Solids and Structures* 46, 3272–3281.
 Moored, K.W., Fish, F.E., Bart-Smith, H., in preparation. Analytical model to describe the pectoral fin kinematics of the manta birostris: implications for bio-inspired design.
 Motro, R., 2003. *Tensegrity: Structural Systems for the Future*, first ed. Kogan Page Science, London.
 Murakami, H., 2001. Static and dynamic analyses of tensegrity structures. Part I. Nonlinear equations of motion. *International Journal of Solids and Structures* 38 (20), 3599–3613.
 Pellegrino, S., 1990. Analysis of prestressed mechanisms. *International Journal of Solids and Structures* 26 (12), 1329–1350.
 Pinaud, J., Masic, M., Skelton, R., 2003. Path planning for the deployment of tensegrity structures. *Smart Structures and Materials* 2003 (5049), 436–447.
 Quirant, J., 2007. Selfstressed systems comprising elements with unilateral rigidity: selfstress states, mechanisms and tension setting. *International Journal of Space Structures* 22 (4), 203–214.
 Quirant, J., Kazi-Aoual, M.N., Laporte, R., 2003. Tensegrity systems: the application of linear programming in search of compatible selfstress states. *Journal of the International Association for Shell and Spatial Structures* 44 (1), 33–50.
 Shea, K., Fest, E., Smith, I., 2002. Developing intelligent tensegrity structures with stochastic search. *Advanced Engineering Informatics* 16 (1), 21–40.
 Skelton, R., de Oliveira, M., 2009. Optimal tensegrity structures in bending: The discrete michell truss. *Journal of the Franklin Institute*.
 Smaili, A., Motro, R., 2005. Folding/unfolding of tensegrity systems by removal of self-stress. In: *International Symposium on Shell and Spatial Structures*, pp. 595–602.
 Sultan, C., Corless, M., Skelton, R.E., 2002. Symmetrical reconfiguration of tensegrity structures. *International Journal of Solids and Structures* 39 (8), 2215–2234.
 Sultan, C., Skelton, R., 2003. Deployment of tensegrity structures. *International Journal of Solids and Structures* 40 (18), 4637–4657.
 Tibert, A., Pellegrino, S., 2003. Deployable tensegrity masts. In: *Proceedings of the 44th AIAA/ASME/ASCE/AHS Structures, Structural Dynamics, and Materials Conference*.
 Tibert, G., 2002. *Deployable Tensegrity Structures for Space Applications*. Royal Institute of Technology.
 Williamson, D., Skelton, R.E., Han, J., 2003. Equilibrium conditions of a tensegrity structure. *International Journal of Solids and Structures* 40 (23), 6347–6367.
 You, Z., Pellegrino, S., 1996. Cable-stiffened pantographic deployable structures. Part 1: Triangular mast. *AIAA Journal* 34 (4), 813–820.
 You, Z., Pellegrino, S., 1997. Cable-stiffened pantographic deployable structures. Part 2: Mesh reflector. *AIAA Journal* 35 (8), 1348–1355.